Received: 31 July 2019 | Revised: 20 December 2019 | Accepted: 21 January 2020

DOI: 10.1111/sapm.12304

Check for updates

STUDIES IN APPLIED MATHEMATICS WILEY

ORIGINAL ARTICLE

# Fronts in two-phase porous media flow problems: The effects of hysteresis and dynamic capillarity

**K. Mitra**[1] | **T. Köppl**[2] | **I. S. Pop**[3,4] | **C. J. van Duijn**[5,6] | **R. Helmig**[7]

[1]Faculty of Mathematics, Technical University of Dortmund, Dortmund, Germany

[2]Department of Mathematics, University of Technology Munich, Garching bei München, Germany

[3]Faculty of Science, Hasselt University, Hasselt, Belgium

[4]Department of Mathematics, University of Bergen, Norway

[5]Department of Earth Sciences, University of Utrecht, Utrecht, The Netherlands

[6]Department of Mechanical Engineering, Eindhoven University of Technology, Eindhoven, The Netherlands

[7]Department of Hydromechanics and Modelling of Hydrosystems, University of Stuttgart, Stuttgart, Germany

**Correspondence**
K. Mitra, Faculty of Mathematics, Technical University of Dortmund, Vogelpothsweg 87, 44227 Dortmund, Germany.
Email: koondanibha.mitra@tu-dortmund.de

**Funding information**
Deutsche Forschungsgemeinschaft, Grant/Award Number: 327154368; Technische Universität Dortmund; Universiteit Hasselt, Grant/Award Number: BOF17BL04; Fonds Wetenschappelijk Onderzoek, Grant/Award Numbers: G051418N, G0G1316N; Darcy Center, Eindhoven University of Technology and Utrecht University; Cluster of Excellence in Simulation Technology, Grant/Award Number: (EXC 310/2); Nederlandse Organisatie voor Wetenschappelijk Onderzoek, Grant/Award Number: 14CSER016

## Abstract

In this work, we study the behavior of saturation fronts for two-phase flow through a long homogeneous porous column . In particular, the model includes hysteresis and dynamic effects in the capillary pressure and hysteresis in the permeabilities. The analysis uses traveling wave approximation. Entropy solutions are derived for Riemann problems that are arising in this context. These solutions belong to a much broader class compared to the standard Oleinik solutions, where hysteresis and dynamic effects are neglected. The relevant cases are examined and the corresponding solutions are categorized. They include non-monotone profiles, multiple shocks, and self-developing stable saturation plateaus. Numerical results are presented that illustrate the mathematical analysis. Finally, we discuss the implication of our findings in the context of available experimental results.

**KEYWORDS**

dynamic capillarity, hysteresis, Riemann problem, traveling waves, two-phase flow

This is an open access article under the terms of the Creative Commons Attribution License, which permits use, distribution and reproduction in any medium, provided the original work is properly cited.

© 2020 The Authors. *Studies in Applied Mathematics* published by Wiley Periodicals, Inc.

# 1 | INTRODUCTION

Modeling of two-phase flow through the subsurface is important for many practical applications, from groundwater modeling and oil and gas recovery to $CO_2$ sequestration. For this purpose, the mass balance equations are used which read in the absence of source terms[1,2] as follows:

$$\phi \frac{\partial \left(\rho_\alpha S_\alpha\right)}{\partial t} + \nabla \cdot \left(\rho_\alpha v_\alpha\right) = 0,\ \alpha \in \{w, n\}, \tag{1}$$

where $\alpha = n$ denotes the nonwetting phase and $\alpha = w$ the wetting phase. Furthermore, $\phi$ is the porosity, $S_\alpha$ and $\rho_\alpha$ the saturation and density of the phases. The phase-velocities $v_\alpha$ are given by the Darcy's law,[1,2]

$$v_\alpha = -\frac{k_{r\alpha}}{\mu_\alpha} K \left(\nabla p_\alpha - \rho_\alpha g \hat{e}_g\right),\ \alpha \in \{w, n\}. \tag{2}$$

Here $K[\mathrm{m}^2]$ is the absolute permeability of the porous medium, $\mu_\alpha[\mathrm{Pa} \cdot \mathrm{s}]$ the viscosity, and $k_{r\alpha}$ the relative permeability of each phase. Moreover, $p_\alpha$ [Pa], $g$ [$\mathrm{m/s}^2$], and $\hat{e}_g$ stand for the phase pressure, the gravitational acceleration, and the unit vector along gravity, respectively. Observe that the system (1)-(2) is not closed as there are more unknowns than equations, that is, $S_\alpha$, $k_{r\alpha}$, and $p_\alpha$. Hence, one needs to take certain assumptions. Assuming incompressibility results in $\rho_\alpha$ being constant. Moreover, by definition

$$S_w + S_n = 1. \tag{3}$$

Commonly it is assumed that the relative permeabilities, as well as the phase pressure difference, are functions of the saturation of the wetting phase,[1,2]

$$k_{rn} = k_{rn}(S_w), \quad k_{rw} = k_{rw}(S_w), \quad \text{and} \quad p_n - p_w = p_c(S_w). \tag{4}$$

The function $p_c : (0, 1] \to \mathbb{R}^+$ is referred to as the capillary pressure function. System (1)-(4) reduces to the hyperbolic Buckley-Leverett equation if this term is neglected, that is, $p_c \equiv 0$. The model given by (1)-(4) works well under close to equilibrium conditions and when flow reversal does not take place. However, some more general cases cannot be explained by this model.

One of the first evidences of deviation from the standard model was reported in the 1931 paper by Richards[3] where he concluded that the capillary pressure term is hysteretic in nature. Capillary hysteresis refers to the phenomenon that $p_c$ measured for a wetting phase infiltration process follows a curve, denoted here by $p_c^{(i)}(S_w)$, which differs from $p_c$ measured for a drainage process, denoted by $p_c^{(d)}(S_w)$. If the process changes from infiltration to drainage or vice versa, then the $p_c$ follows scanning curves that are intermediate to $p_c^{(i)}(S_w)$ and $p_c^{(d)}(S_w)$.[4] This is shown in detail in Figure 1 (left). Since then, hysteresis has been studied experimentally,[5-7] analytically,[8-12] and numerically.[12-16] Variety of models have been proposed to incorporate the effects of hysteresis, such as independent and dependent domain models[17-19] and interfacial area models.[20-23] A comprehensive study of these models can be found in Ref. 24. Using thermodynamically constrained averaging theory (TCAT),[25,26] one can eliminate hysteresis in capillary pressure altogether by introducing interfacial area and Euler characteristics as additional unknowns. A mathematical study of such models is undoubtedly interesting. However, they require additional constitutive equations. Thus, their analysis is beyond the scope of the present work. In this paper, we will use the play-type hysteresis model[4,24] that approximates scanning curves as constant saturation lines. Such models are generally implemented

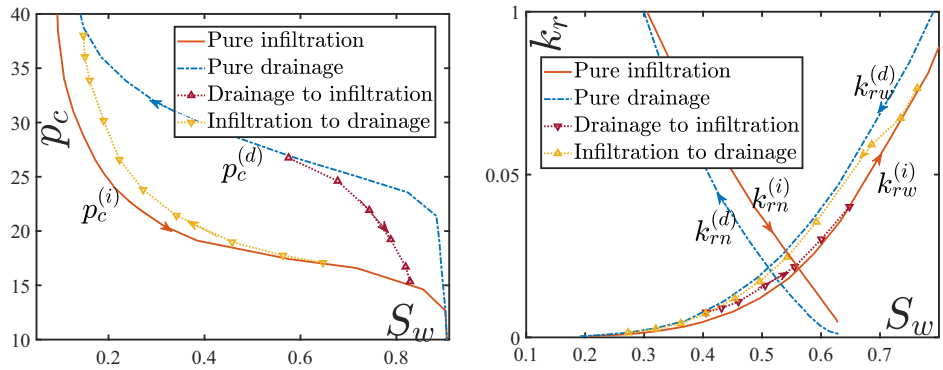


**FIGURE 1** (Left) Hysteresis of capillary pressure and scanning curves. The plots drawn use data points from figs. 4 and 5 of Ref. 5. (Right) Hysteresis of relative permeabilities. Experimental data from Ref. 32 are used for the $k_{rw}$ plots and the corresponding scanning curves. Plots for $k_{rn}$ show data from Ref. 29. The curves are scaled in the $y$-direction

in classical porous media simulators. Well-posedness results for play-type hysteresis model are found in Refs. 8, 9, 11, 12, 27. It has a physical basis[4,28] and it can be extended to depict the realistic cases accurately.[24] A similar hysteretic behavior is observed for the relative permeabilities too, although to a lesser extent. Hysteresis of the nonwetting phase relative permeability in the two-phase case (oil and water for example) is reported in Refs. 29-31. The wetting permeability $k_{rw}$ also exhibits hysteresis[6,32] but the effect is less pronounced (see Figure 1 (right)).

Another effect that cannot be explained by the standard model is the occurrences of overshoots. More precisely, in infiltration experiments through initially low saturated soils, it is observed that if the flow rate is large enough then the saturation at an interior point is larger than that on the boundary even in the absence of internal sources.[33-35] This cannot be explained by a second-order model such as (1)-(4).[36-38] Hence, based on thermodynamic considerations the dynamic capillary model was proposed in Ref. 39. Since then the dynamic capillary term has been measured experimentally[40,41] and it was used successfully to explain overshoots.[9,11,12,42-45] Also the well-posedness of the dynamic capillarity model has been proved[46-49] and numerical methods have been investigated.[50-54]

In this paper, we are interested in studying how the flow behavior is influenced if one considers the nonequilibrium effects, that is, hysteresis and dynamic capillarity. For this purpose, we study the system in a one-dimensional setting. The one-dimensional case is relevant when one spatial direction is dominant; it approximates flow through viscous fingers[12,55,56] and it can explain results from the standard experimental setting shown in Figure 2.[33-35] In this study, the behavior of the fronts is investigated by traveling wave (TW) solutions. The TW solutions can approximate the saturation and pressure profiles in infiltration experiments through a long column, and the existence conditions of the TWs act as the entropy conditions for the corresponding hyperbolic model when the viscous terms are disregarded. For the unsaturated case ($p_n = 0$), TW solutions with dynamic effect were analyzed in Ref. 42 For the two-phase case, it was shown rigorously in Refs. 43, 44, 57 that nonmonotone TWs and nonstandard entropy solutions are existing if one includes dynamic capillarity effect. Similar analysis but for higher-order viscous terms containing spatial derivatives were performed in Refs. 58, 59. The existence of TW solutions for the unsaturated case when dynamic capillarity and capillary hysteresis are present was proved in Refs. 9, 45 and criteria for nonmonotonicity and reaching full saturation were stated. It is evidenced in Refs. 15, 60 that hysteresis can explain stable saturation plateaus but it cannot initiate them. In Refs. 10, 12, it is shown how both hysteresis and dynamic capillarity are

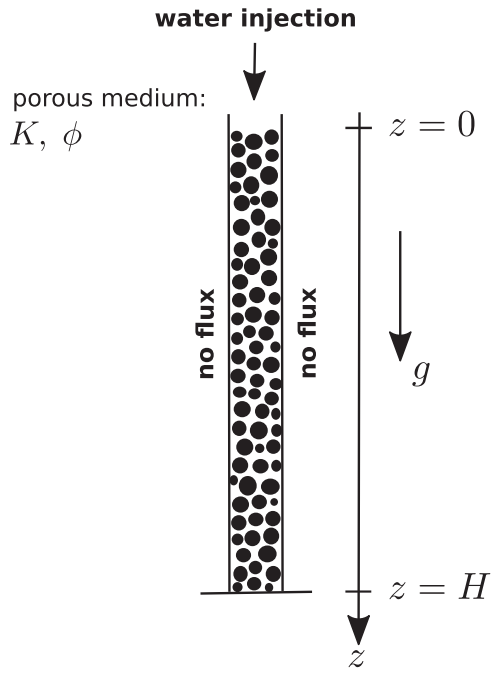


**FIGURE 2** Setup of an infiltration experiment. Water is injected at a constant rate at the inlet of a column having height $H$. The main axis of the column is orientated along the gravity vector

required to explain the growth of viscous fingers. The entropy conditions for Buckley-Leverett equation considering hysteresis in only permeability were derived in Refs. 61-63. However, hysteresis and nonlinearities were not included in the viscous term. This is taken into consideration in Ref. 64 where the authors add a dynamic term to model permeability hysteresis, while disregarding hysteresis and dynamic effects in capillary pressure. The behavior of TW for a nonmonotone flux function in the presence of a third-order term was described in Ref. 65.

In our current work, we build upon[9,42-45] to describe the behavior of fronts in the two-phase case when dynamic capillarity and both type of hysteresis are included. The models that are used in our analysis are introduced in Section 2. Section 3 discusses the existence of TWs when hysteresis and dynamic effects are included in the capillary pressure but not in the permeabilities. Entropy conditions are derived and they reveal that there can be nonclassical shocks. In Section 4, the analysis is extended to include hysteresis in the permeabilities. This makes self-developing stable saturation plateaus and a broader class of entropy solutions possible. Section 5 presents numerical results that support our analytical findings. Finally, we make some concluding remarks in Section 6 and compare the results with experiments.

## 2 | MATHEMATICAL MODEL

This section is dedicated to the formulation of a mathematical model that can be used to describe an infiltration process of a fluid into a homogeneous porous column. An example for such an infiltration process is the injection of water into a dry sand column (see Figure 2).

## 2.1 | Governing equations

Here we consider the one-dimensional situation where the flow problem is defined on an interval $(0, H)$. This simplification is justified by the fact that the walls of the porous column, in which the fluids are injected are impermeable and that saturation is in general almost constant across the section area of the column. The axis is pointing in the direction of gravity. The medium is assumed to be homogeneous and the fluids are incompressible. Under these constraints, (1)-(2) simplify to

$$\phi \frac{\partial S_\alpha}{\partial t} + \frac{\partial v_\alpha}{\partial z} = 0, \quad v_\alpha = -\frac{k_{r\alpha}}{\mu_\alpha} K \left( \frac{\partial p_\alpha}{\partial z} - \rho_\alpha g \right), \quad \alpha \in \{w, n\}, \tag{5}$$

where $t$ and $z$ are denoting the time and space variables, respectively. To further simplify the model, after summing (5) for the two phases and using (3) we observe that the total velocity

$$v(z,t) = v_w(z,t) + v_n(z,t) \tag{6}$$

is constant in space. In addition to that, we assume that $v$ is also constant in time, which occurs, for example, if a constant influx (injection rate) is prescribed at the inlet $z = 0$. This gives

$$\frac{\partial v}{\partial t} = \frac{\partial v}{\partial z} = 0, \quad \text{or} \quad v(z,t) \equiv v \text{ for } z \in (0, H) \quad \text{and } t > 0. \tag{7}$$

From (5)-(7), one finds

$$v_w = \frac{k_{rw}}{k_{rw} + \frac{\mu_w}{\mu_n} k_{rn}} v + \frac{K}{\mu_n} \frac{k_{rw} k_{rn}}{k_{rw} + \frac{\mu_w}{\mu_n} k_{rn}} \left( \frac{\partial p_c}{\partial z} + \left( \rho_w - \rho_n \right) g \right). \tag{8}$$

At this stage, we define the fractional flow function

$$f := \frac{k_{rw}}{k_{rw} + \frac{\mu_w}{\mu_n} k_{rn}}, \tag{9}$$

and the function

$$h := \frac{k_{rw} k_{rn}}{k_{rw} + \frac{\mu_w}{\mu_n} k_{rn}} = k_{rn} f. \tag{10}$$

Substituting these relations and definitions into (5) for $\alpha = w$ yields the transport equation for the wetting phase

$$\frac{\partial S}{\partial t} + \frac{v}{\phi} \frac{\partial}{\partial z} \left[ f + \frac{K \left( \rho_w - \rho_n \right) g}{v \mu_n} h + \frac{K}{v \mu_n} h \frac{\partial p}{\partial z} \right] = 0, \tag{11}$$

where we used the notation

$$S := S_w \quad \text{and} \quad p := p_n - p_w. \tag{12}$$

Note that $f$ and $h$ are functions of $S$ and possibly of $p$, as shown below.

## 2.2 | Modeling hysteresis and dynamic capillarity

To incorporate hysteresis and dynamic capillarity in the model, one needs to extend capillary pressure and relative permeability given in the closure relationship (4).

### 2.2.1 | Capillary pressure

The following expression is used to extend the capillary pressure:

$$p \in \frac{1}{2}\left(p_c^{(i)}(S) + p_c^{(d)}(S)\right) - \frac{1}{2}\left(p_c^{(d)}(S) - p_c^{(i)}(S)\right) \cdot \operatorname{sign}\left(\frac{\partial S}{\partial t}\right) - \tau \frac{\partial S}{\partial t}, \tag{13}$$

where sign(·) denotes the multivalued signum graph

$$\operatorname{sign}(\xi) = \begin{cases} 1, & \text{for } \xi > 0, \\ [-1, 1], & \text{for } \xi = 0, \\ -1, & \text{for } \xi < 0 \end{cases} \tag{14}$$

(see Refs. 4, 11, 39). The second and third terms in the right-hand side of (13) describe, respectively, capillary hysteresis[4] and dynamic capillarity.[39] Furthermore, $\tau \geq 0$ denotes the dynamic capillary coefficient. It models relaxation or damping in the capillary pressure. Although in practice $\tau$ may depend on $S$,[34,40] here we assume it to be constant. The case of nonconstant $\tau$ is considered in Refs. 9, 45. The capillary pressure functions $p_c^{(j)}$, $j \in \{i, d\}$, fulfill[1,2,5]:

(P1) $p_c^{(j)} : (0, 1] \to [0, \infty)$, $p_c^{(j)} \in C^1((0, 1])$, $p_c^{(j)}(1) = 0$. Moreover, $p_c^{(j)\prime}(S) < 0$ and $p_c^{(i)}(S) < p_c^{(d)}(S)$ for $S \in (0, 1)$.

Here, and later in this paper, a prime denotes differentiation with respect to the argument. In the absence of dynamic effects, that is, $\tau = 0$, expression (13) implies

$$p = \begin{cases} p_c^{(i)}(S) & \text{when } \partial_t S > 0, \\ p_c^{(d)}(S) & \text{when } \partial_t S < 0. \end{cases}$$

This is precisely what is seen from water infiltration/drainage experiments.[5] When $\frac{\partial S}{\partial t} = 0$, $p$ is between $p_c^{(i)}(S)$ and $p_c^{(d)}(S)$. For this reason, the hysteresis described by (13) is called play-type hysteresis: that is, the scanning curves between $p_c^{(i)}(S)$ and $p_c^{(d)}(S)$ are vertical.

Before discussing the case $\tau > 0$, we introduce for convenience the sets

$$\mathcal{H}^{(i)} := \left\{(S, p) : S \in (0, 1],\ p < p_c^{(i)}(S)\right\}, \tag{15a}$$

$$\mathcal{H}^{(d)} := \left\{(S, p) : S \in (0, 1],\ p > p_c^{(d)}(S)\right\}, \tag{15b}$$

$$\mathcal{H} := \left\{(S, p) : S \in (0, 1],\ p_c^{(i)}(S) \leq p \leq p_c^{(d)}(S)\right\}, \tag{15c}$$

and the strip $\mathcal{W} = \mathcal{H}^{(i)} \cup \mathcal{H} \cup \mathcal{H}^{(d)} = \{0 < S \leq 1\}$. In Ref. 45, it is shown that pressure expression (13) can be written as

$$\frac{\partial S}{\partial t} = \frac{1}{\tau}\mathcal{F}(S,p) := \frac{1}{\tau}\begin{cases} p_c^{(d)}(S) - p & \text{if } (S,p) \in \mathcal{H}^{(d)}, \\ 0 & \text{if } (S,p) \in \mathcal{H}, \\ p_c^{(i)}(S) - p & \text{if } (S,p) \in \mathcal{H}^{(i)}. \end{cases} \tag{16}$$

### 2.2.2 | Relative permeability

To make the effect of hysteresis explicit in the relative permeabilities, we need to incorporate a dependence on both $S$ and $\frac{\partial S}{\partial t}$. This dependence should satisfy

$$k_{r\alpha}\Big(S, \frac{\partial S}{\partial t}\Big) = \begin{cases} k_{r\alpha}^{(i)}(S) & \text{if } \frac{\partial S}{\partial t} > 0, \\ k_{r\alpha}^{(d)}(S) & \text{if } \frac{\partial S}{\partial t} < 0, \end{cases} \text{ for } \alpha \in \{w, n\}. \tag{17}$$

Here, $k_{r\alpha}^{(i)}, k_{r\alpha}^{(d)} : [0,1] \to \mathbb{R}$ are the infiltration and drainage relative permeabilities obtained from experiments.[6,29-32] In line with the experimental outcomes, we assume here for $j \in \{i, d\}$,

(P2) $k_{rw}^{(j)} \in C^2([0,1])$, $k_{rw}^{(j)\prime}(S) > 0$ for $0 < S \leq 1$, $k_{rw}^{(j)}(0) = 0$ and $k_{rw}^{(j)}$ is strictly convex. Moreover, for $0 < S < 1$, $k_{rw}^{(i)}(S) < k_{rw}^{(d)}(S)$.

(P3) $k_{rn}^{(j)} \in C^2([0,1])$, $k_{rn}^{(j)\prime}(S) < 0$ for $0 \leq S < 1$, $k_{rn}^{(j)}(1) = 0$ and $k_{rn}$ is strictly convex. Moreover, for $0 < S < 1$, $k_{rn}^{(d)}(S) < k_{rn}^{(i)}(S)$.

Note the reverse ordering in $k_{rw}$ and $k_{rn}$ when switching from infiltration to drainage. This is demonstrated experimentally in Refs. 29, 30, 32, see also Figure 1.

In Ref. 66, a play-type approach has been proposed to model $k_{r\alpha}$ where

$$k_{r\alpha} \in \frac{1}{2}\big(k_{r\alpha}^{(d)}(S) + k_{r\alpha}^{(i)}(S)\big) - \frac{1}{2}\big(k_{r\alpha}^{(d)}(S) - k_{r\alpha}^{(i)}(S)\big) \cdot \operatorname{sign}\Big(\frac{\partial S}{\partial t}\Big). \tag{18}$$

However, this model is ill-posed in the unregularized case as for $\frac{\partial S}{\partial t} = 0$ the relative permeabilities are undetermined, that is, the relative permeabilities have no equation to determine them when $\frac{\partial S}{\partial t} = 0$. This is different for the capillary pressure (13) because $p$ satisfies Equation (11) as well. With the permeabilities, we take an approach inspired by Refs. 61-63. Here, inherited from the capillary pressure, the hysteresis is of the play-type as well, but now depending on $S$ and $p$, rather than on $S$ and $\frac{\partial S}{\partial t}$. We propose the following model: for $\alpha \in \{w, n\}$

$$k_{r\alpha} = k_{r\alpha}(S,p) = \begin{cases} k_{r\alpha}^{(d)}(S) & \text{if } (S,p) \in \mathcal{H}^{(d)}, \\ \bar{k}_{r\alpha}(S,p) & \text{if } (S,p) \in \mathcal{H}, \\ k_{r\alpha}^{(i)}(S) & \text{if } (S,p) \in \mathcal{H}^{(i)}. \end{cases} \tag{19}$$

Here, $\bar{k}_{r\alpha} : \mathcal{H} \to [0, \infty)$ is a given function that satisfies

(P4) $\bar{k}_{r\alpha} \in C^2(\mathcal{H})$ such that $k_{r\alpha} \in C(\mathcal{W})$ for $\alpha \in \{w, n\}$ and $\partial_p \bar{k}_{rw} > 0$, $\partial_p \bar{k}_{rn} < 0$ in $\mathcal{H}$.

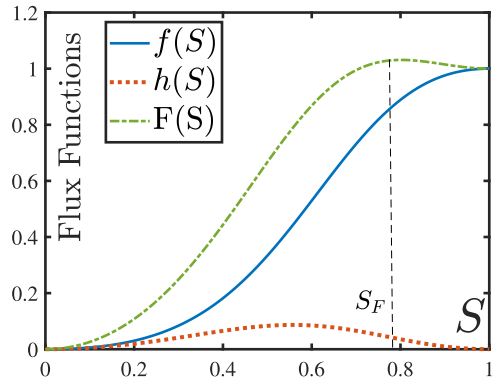


**FIGURE 3** The functions $f(S)$, $h(S)$, and $F(S)$ as given in Remark 2. Here, $M = 2$ and $N_g = 4$

Observe that this implies $\bar{k}_{r\alpha}(S, p_c^{(j)}(S)) = k_{r\alpha}^{(j)}(S)$ for $j \in \{i, d\}$. For the moment we leave the choice of $\bar{k}_{r\alpha}$ unspecified except for properties (P4), as it neither influences the entropy conditions nor the critical $\tau$ values introduced afterward.

*Remark* 1. In the computations, one needs to specify an expression for $\bar{k}_{r\alpha}$. In Section 5, we use

$$\bar{k}_{r\alpha}(S, p) = k_{r\alpha}^{(i)}(S) + \left(k_{r\alpha}^{(d)}(S) - k_{r\alpha}^{(i)}(S)\right)\left(\frac{p - p_c^{(i)}(S)}{p_c^{(d)}(S) - p_c^{(i)}(S)}\right). \tag{20}$$

This expression is obtained by considering sign in (13) and (18) as a function that can be eliminated. With $\tau = 0$ in (13), this results in (20). Since the fraction (20) is bounded by 0 and 1 for $(S, p) \in \mathcal{H}$, we have $\lim_{S \searrow 0} k_{r\alpha}(S, p) = k_{r\alpha}^{(i)}(0) = k_{r\alpha}^{(d)}(0)$ and similar for $S \nearrow 1$.

Observe that (19) is consistent with (17) as from (16), $\frac{\partial S}{\partial t} > 0$ iff $p < p_c^{(i)}(S)$ and $\frac{\partial S}{\partial t} < 0$ iff $p > p_c^{(d)}(S)$. Moreover, the scanning curves for $k_{r\alpha}$ have constant $S$. Although not true in general, see, for instance, Figure 1, we restrict ourselves to play-type for both $p$ and $k_{r\alpha}$. An extension describing nonvertical scanning curves is discussed in Ref. 24 and chapters 3,11 of Ref. 27.

Using (19) and (9),(10), the nonlinearities $f$ and $h$ are expressed in terms of $S$ and $p$ as well:

$$\zeta(S, p) = \begin{cases} \zeta^{(d)}(S) & \text{if } (S, p) \in \mathcal{H}^{(d)}, \\ \bar{\zeta}(S, p) & \text{if } (S, p) \in \mathcal{H}, \\ \zeta^{(i)}(S) & \text{if } (S, p) \in \mathcal{H}^{(i)}, \end{cases} \quad \text{for } \zeta \in \{f, h\}. \tag{21}$$

From (P2)-(P4) we deduce for $f$ and $h$:

(P5) $f \in C(\mathcal{W})$, $\bar{f} \in C^2(\mathcal{H})$ and $\partial_p \bar{f} > 0$ in $\mathcal{H}$. For $j \in \{i, d\}$, $f^{(j)} \in C^2([0, 1])$, $f^{(j)'}(S) > 0$ for $0 < S < 1$, $f^{(j)}(0) = 0$, $f^{(j)}(1) = 1$. Moreover, for $0 < S < 1$, $f^{(i)}(S) < f^{(d)}(S)$.

(P6) $h \in C(\mathcal{W})$, $\bar{h} \in C^2(\mathcal{H})$, $h^{(j)} \in C^2([0, 1])$ and $h^{(j)}(0) = h^{(j)}(1) = 0$ for $j \in \{i, d\}$.

Observe that in general no ordering holds between $h^{(i)}$ and $h^{(d)}$. Typical curves for $f^{(j)}$ and $h^{(j)}$ are shown in Figure 3. The Equations (11), (13), and (21) are the complete set of equations for our model.

## 2.3 | Dimensionless formulation

Let $H$ [m] be the characteristic length, $p_r$ [Pa] the characteristic pressure, $t_r = \frac{\phi H}{v}$[s] the characteristic time, and $\tau_r$[Pa · s] the characteristic dynamic capillary constant. Inspired by the J-Leverett model,[67] we take as characteristic pressure $p_r = \sigma\sqrt{\frac{\phi}{K}}$, $\sigma$ being the surface tension between the two phases. Alternatively, one could consider $p_r = (\rho_n - \rho_w)gH$ which is a more common choice for the Richards equation with gravity. Setting

$$\tilde{z} := \frac{z}{H}, \quad \tilde{t} := \frac{t}{t_r}, \quad \tilde{\psi} := \frac{\psi}{p_r}, \quad \text{and} \quad \tilde{\tau} = \frac{\tau}{\tau_r},$$

where $\psi \in \{p, p_c^{(i)}, p_c^{(d)}\}$, and defining the dimensionless numbers

$$N_g := \frac{K(\rho_w - \rho_n)g}{v\mu_n} \text{ (gravity number) and } N_c := \frac{Kp_r}{v\mu_n H} \text{ (capillary number),}$$

we obtain from (11) the dimensionless transport equation

$$\frac{\partial S}{\partial \tilde{t}} + \frac{\partial}{\partial \tilde{z}}\left(f + N_g h + N_c h \frac{\partial \tilde{p}}{\partial \tilde{z}}\right) = 0. \tag{22}$$

The closure relation (13) becomes

$$\tilde{p} \in \frac{1}{2}\left(\tilde{p}_c^{(i)}(S) + \tilde{p}_c^{(d)}(S)\right) - \frac{1}{2}\left(\tilde{p}_c^{(d)}(S) - \tilde{p}_c^{(i)}(S)\right) \cdot \operatorname{sign}\left(\frac{\partial S}{\partial \tilde{t}}\right) - \tilde{\tau}\frac{\tau_r}{p_r t_r}\frac{\partial S}{\partial \tilde{t}}. \tag{23}$$

Now choosing $\tau_r = N_c p_r t_r = p_r^2 \frac{\phi K}{v^2 \mu_n}$, the Leverett scaling for $p_r$ gives

$$\tau_r = \frac{\sigma^2 \phi^2}{\mu_n v^2} \text{ implying } \tilde{\tau} = \frac{\mu_n v^2}{\sigma^2 \phi^2}\tau. \tag{24}$$

This choice leaves us with a characteristic dynamic coefficient that is independent of the length scale of the problem. This is precisely the scaling used in Refs. 43, 44, 68 that is consistent with the hyperbolic limit. Realistic values of dimensional and scaled quantities are given in Ref. 69.

Dropping the ˜ sign from the notation, we are left with the dimensionless system

$$(\mathcal{P}) \begin{cases} \dfrac{\partial S}{\partial t} + \dfrac{\partial}{\partial z}\left(F(S,p) + N_c h(S,p)\dfrac{\partial p}{\partial z}\right) = 0, & \text{(25a)} \\ \dfrac{\partial S}{\partial t} = \dfrac{1}{N_c \tau}\mathcal{F}(S,p), & \text{(25b)} \end{cases}$$

$$\text{where } F = f + N_g h. \tag{25c}$$

This system can be seen as a regularization of the hyperbolic Buckley-Leverett equation with gravity. Here, the regularization involves hysteresis and dynamic capillarity. Compared to the usual second-order parabolic regularization, yielding shocks that satisfy the standard Oleinik conditions,[70] different (nonparabolic) regularizations may yield shocks that violate these conditions, see, for example, Refs. 43, 71. Such shocks are called nonclassical.

One of the main issues that concerns this paper is to show the existence of nonclassical shocks originating from System ($\mathcal{P}$). To this end, we proceed as in Ref. 43 and study the existence of TW

solutions of ($\mathcal{P}$) that connect a left state $S_B$ to a right state $S_T$ in the presence of both hysteresis and dynamic capillarity. TWs for the model with only dynamic capillarity are analyzed in Refs. 44, 57. For the case of unsaturated flow, that is, Richards equation with a convex flux function, existence and qualitative properties of TWs are considered in detail in Refs. 9, 42, 45.

For the purpose of TWs, we consider System ($\mathcal{P}$) in the domain $-\infty < z < \infty$. Then the capillary number $N_c$ can be removed from the problem by the scaling

$$z := z/N_c \text{ and } t := t/N_c.$$

This yields the $N_c$ independent formulation

$$(\tilde{\mathcal{P}})\begin{cases} \dfrac{\partial S}{\partial t} + \dfrac{\partial}{\partial z}\left( F(S,p) + h(S,p)\dfrac{\partial p}{\partial z}\right) = 0, \\ \dfrac{\partial S}{\partial t} = \dfrac{1}{\tau}\mathcal{F}(S,p), \end{cases} \tag{26}$$

with $-\infty < z < \infty$ and $t > 0$. This is the starting point for the TW analysis.

*Remark* 2. Using the Brooks-Corey type expression, for example, see Ref. 72,

$$k_{rw}(S) = S^q \text{ and } k_{rn}(S) = (1-S)^q, \tag{27}$$

with $q = 2$, the nonlinearities (9), (10), and (25c) become for no-hysteresis in permeabilities,

$$f(S) = \frac{S^2}{S^2 + M(1-S)^2}, \quad h(S) = (1-S)^2 f(S), \quad F(S) = S^2\frac{(1 + N_g(1-S)^2)}{S^2 + M(1-S)^2},$$

where $M = \frac{\mu_w}{\mu_n}$ denotes the viscosity ratio. A plot is shown in Figure 3 for these functions. Some elementary calculations give

(*a*) *Monotonicity*: If $N_g \le M$ then $F'(S) > 0$ for all $0 < S < 1$ and if $N_g > M$ then there exists a unique $S_F \in (0,1)$ such that $F'(S) > 0$ for all $0 < S < S_F$ and $F'(S) < 0$ for $S_F < S < 1$. Since $F(1) = 1$, clearly $F(S_F) > 1$.

(*b*) *Inflection points*: $f(S)$ has only one inflection point in (0,1) whereas, $F(S)$ has at most two. To see this for $f(S)$, note that $f''(S) = P(S)Q(S)$ with $Q(S)$ being a positive function and $P(S) = M - (3M+3)S^2 + (2M+2)S^3$. Since $P(0) = M$, $P(1) = -1$ and $P'(S) < 0$ for $S \in (0,1)$, the result follows.

These properties of $f$ and $F$ will be used when discussing the different cases of TWs.

## 2.4 | TW formulation

Having derived the nondimensional hysteretic two-phase flow System ($\tilde{\mathcal{P}}$), we investigate under which conditions TW solutions exist. These are solutions of the form

$$S(z,t) = S(\xi),\ p(z,t) = p(\xi), \text{ with } \xi = ct - z,$$

where $S$ and $p$ are the wave profiles of saturation and pressure and $c \in \mathbb{R}$ the wave-speed. We seek TWs that satisfy

$$\begin{cases} \lim_{\xi\to-\infty} S(\xi) = S_B, \ \lim_{\xi\to\infty} S(\xi) = S_T, \\ \lim_{\xi\to-\infty} p'(\xi) = \lim_{\xi\to\infty} p'(\xi) = 0, \end{cases} \tag{28}$$

where $S_B$ corresponds to an "initial" saturation and $S_T$ to the injected saturation. The choice of $p'(\pm\infty) = 0$ ensures that the diffusive flux vanishes at $\xi = \pm\infty$. Substituting (28) into (26), and integrating (26) one obtains

$$cS - \left(F(S,p) - h(S,p)p'\right) = A, \tag{29a}$$

$$cS' = \frac{1}{\tau}\mathcal{F}(S,p), \tag{29b}$$

where $\xi \in \mathbb{R}$ and $A$ is a constant of integration.

As was shown in Ref. 9 for the Richards equation, (28) and (29) do not automatically guarantee the existence of $\lim_{\xi\to\pm\infty} p(\xi)$. However, if $p(\pm\infty)$ is well-defined then (29b) and the existence of $S(\pm\infty)$ forces $\lim_{\xi\to\pm\infty} \mathcal{F}(S(\xi), p(\xi)) = 0$. Recalling that $\mathcal{F}(S,p) = 0$ iff $(S,p) \in \mathcal{H}$ we then have

$$\lim_{\xi\to-\infty} p(\xi) = p_B \in \left[p_c^{(i)}(S_B), p_c^{(d)}(S_B)\right], \quad \lim_{\xi\to\infty} p(\xi) = p_T \in \left[p_c^{(i)}(S_T), p_c^{(d)}(S_T)\right].$$

We show later that $p_B$, interpreted as the initial pressure, can sometimes be chosen independently, whereas, $p_T$, when existing, is always fixed by the choice of $S_B, S_T$, and $p_B$. Following the steps in Refs. 9, 44, 45, we obtain the Rankine-Hugoniot condition for wave-speed $c$, that is,

$$c = \frac{F(S_T,p_T) - F(S_B,p_B)}{S_T - S_B}. \tag{30}$$

With this, system (29) can be rewritten as a dynamical system,

$$\text{(TW)} \begin{cases} S' = \frac{1}{c\tau}\mathcal{F}(S,p), \\ p' = \mathcal{G}(S,p), \end{cases} \tag{31}$$

where

$$\mathcal{G}(S,p) := \frac{F(S,p) - \ell(S)}{h(S,p)} \quad \text{with} \quad \ell(S) := F(S_B,p_B) + c(S - S_B). \tag{32}$$

Note that when $F$ is nonmonotone (eg, $N_g > M$ in Figure 2), the wave-speed $c$ can be positive or negative depending on the values of $S_B$ and $S_T$.

We study all possible solutions of system (TW) for $\tau > 0$. They serve as viscous profiles of admissible shocks of the limiting Buckley-Leverett equation. Existence conditions for solutions of (TW) act as admissibility/entropy conditions for the corresponding shocks.

The solutions of (TW) are investigated under two different scenarios.

A: No hysteresis in relative permeabilities, that is, $\zeta^{(i)} = \zeta^{(d)}$ for $\zeta \in \{f, h\}$. Furthermore, $N_g$ is sufficiently small so that $F$ satisfies properties stated for $f^{(j)}$ in (P5). For $F$ as in Remark 2 this is satisfied if $N_g \le M$.

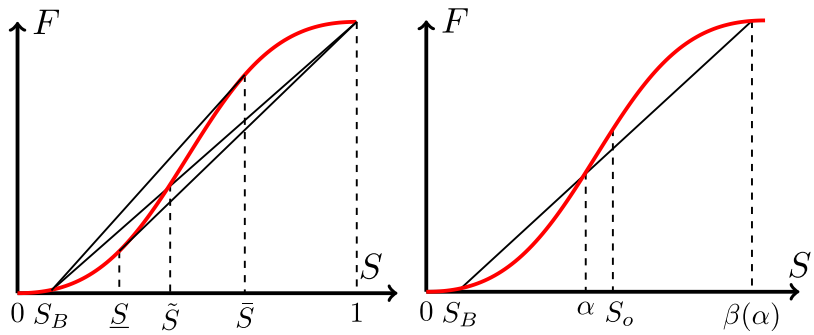


**FIGURE 4** (Left) The saturations $S_B$, $\underline{S}$, $\bar{S}$, and $\tilde{S}$. Here, $\underline{S}$ is the tangent to the $F(S)$ curve from (1,1) and $\bar{S}$ is the tangent from $(S_B, F(S_B))$. (Right) The saturation $\beta(\alpha)$ is defined by the third intersection of the line connecting $(\alpha, F(\alpha))$ and $(S_B, F(S_B))$ with $F$. The inflection point of $F$ is at $S = S_o$ and $\beta(\tilde{S}) = 1$

B: $N_g$ and $\tau$ sufficiently small; relative permeabilities are hysteretic.

A third scenario where $N_g$ is large so that $F$ is nonmonotone is discussed briefly at the end of Section 3.

## 3 | NO RELATIVE PERMEABILITY HYSTERESIS AND SMALL $N_g$ (SCENARIO A)

In the absence of relative permeability hysteresis, the functions $f$, $h$, $F$, and $\mathcal{G}$ depend on $S$ only. We explicitly state the properties of $F$ as a result of (P5), (P6), and Remark 2.

(A1) $F \in C^2([0,1])$, $F'(S) > 0$ for $0 < S < 1$, $F(0) = 0$, $F(1) = 1$. Moreover, a unique $S_o \in (0,1)$ exists such that

$$F''(S_o) = 0,\ F''(S) > 0 \text{ for } 0 < S < S_o, \text{ and } F''(S) < 0 \text{ for } S_o < S < 1.$$

### 3.1 | Preliminaries

For the purpose of readability, we moved the proofs of most details in Appendix A. Throughout this section, we restrict ourselves to relatively small values of $S_B$. Specifically, we assume

$$0 < S_B < S_o. \tag{33}$$

First let us take $S_B \le \underline{S}$, where $\underline{S}$ is the saturation at which $F'(\underline{S}) = \frac{1-F(\underline{S})}{1-\underline{S}}$. The convex-concave behavior of $F$ implies $\underline{S} < S_o$. For later purpose, and with reference to Figure 4 (left), we introduce the additional saturations $S_B < \tilde{S} < \bar{S} < 1$, where $\tilde{S}$ is the saturation at which $F(S)$ intersects the line connecting $(S_B, F(S_B))$ and (1,1), and where $\bar{S}$ is the saturation for which $F'(\bar{S}) = \frac{F(\bar{S})-F(S_B)}{\bar{S}-S_B}$. To each $\alpha \in [\tilde{S}, \bar{S}]$ corresponds a unique $\beta \in [\bar{S}, 1]$ such that $(\beta, F(\beta))$ is the third intersection point between the graph of $F$ and the chord through $(S_B, F(S_B))$ and $(\alpha, F(\alpha))$ (see Figure 4 (right)). This

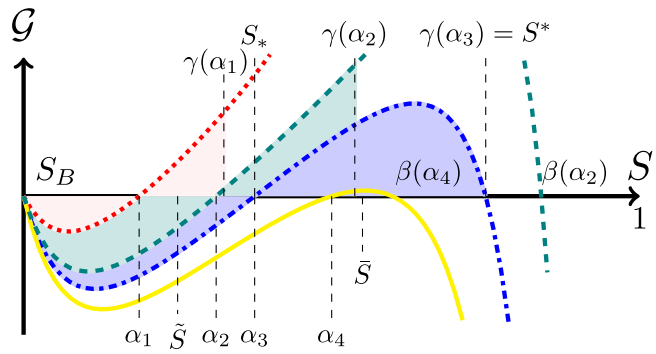


**FIGURE 5** The plot of $\mathcal{G}(S; S_B, \alpha)$ for different values of $\alpha$. Here, $\alpha_1 < \tilde{S} < \alpha_2 < \alpha_3 = S_* < \alpha_4 < \bar{S} < S^*$. Values of $\gamma$ and $\beta$ are also shown. Note that $\beta(\alpha_1)$ and $\gamma(\alpha_4)$ do not exist

defines the function

$$\begin{cases} \beta : [\tilde{S}, \bar{S}] \to [\bar{S}, 1], \ \beta(\bar{S}) = \bar{S}, \ \beta(\tilde{S}) = 1, \\ \beta(\alpha) \text{ is strictly decreasing.} \end{cases} \tag{34}$$

Later in this section, a second function $\gamma = \gamma(\alpha)$ is introduced as one of the roots of the equation

$$\int_{S_B}^{\gamma(\alpha)} \mathcal{G}(S; S_B, \alpha) dS = 0 \text{ for } S_B \le \alpha \le \bar{S}. \tag{35}$$

Here, $\mathcal{G}(S; S_B, \alpha)$ is the expanded notation of $\mathcal{G}$ from (32) for the $p$ independent case:

$$\mathcal{G}(S; S_B, \alpha) = \frac{F(S) - \ell(S; S_B, \alpha)}{h(S)} \quad \text{with} \quad \ell(S; S_B, \alpha) = F(S_B) + \frac{F(\alpha) - F(S_B)}{\alpha - S_B}(S - S_B).$$

A typical sketch of $\mathcal{G}(S; S_B, \alpha)$ for different values of $\alpha$ is shown in Figure 5. Note that

$$\mathcal{G}(S; S_B, \alpha) \text{ decreases with respect to } \alpha \in [S_B, \bar{S}] \text{ and} \tag{36}$$

$$\mathcal{G}(S; S_B, \alpha) \begin{cases} \left.\begin{array}{ll} < 0 & \text{for } S_B < S < \alpha \\ > 0 & \text{for } S > \alpha \end{array}\right\} & \text{when } S_B < \alpha < \tilde{S}, \\ \left.\begin{array}{ll} < 0 & \text{for } S_B < S < \alpha \\ > 0 & \text{for } \alpha < S < \beta(\alpha) \\ < 0 & \text{for } \beta(\alpha) < S < 1 \end{array}\right\} & \text{when } \tilde{S} < \alpha < \bar{S}. \end{cases} \tag{37}$$

Since,

$$\mathcal{G}(S; S_B, \alpha) = \begin{cases} \mathcal{O}\left(\frac{1}{k_{rn}(S)}\right) & \text{when } \alpha \neq \tilde{S}, \\ \mathcal{O}\left(\frac{1-S}{k_{rn}(S)}\right) & \text{when } \alpha = \tilde{S}, \end{cases} \tag{38}$$

as $S \nearrow 1$, we have for most practical applications

$$\mathcal{G}(S; S_B, \alpha) \text{ is nonintegrable near } S = 1 \text{ for each } S_B \le \alpha \le \bar{S}. \tag{39}$$

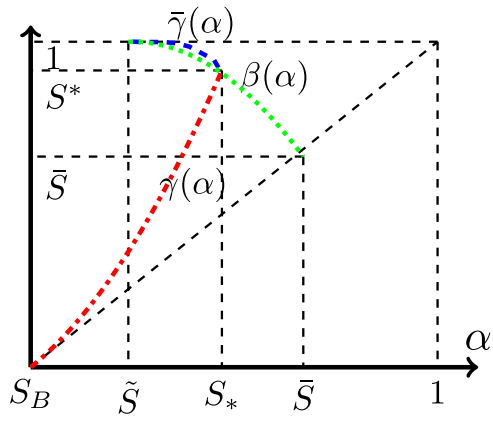


**FIGURE 6** The functions $\beta$, $\gamma$, and $\bar{\gamma}$ (assuming (39)) and the definitions of $S_*$ and $S^*$ for $S_B < \underline{S}$

This is the case for Brooks-Corey permeabilities with $q \geq 2$ (see Remark 2).

*Remark* 3. We also note that in the context of this section the wave-speed (30) reduces to

$$c = \frac{F(S_T) - F(S_B)}{S_T - S_B}.$$

From assumption A1, it follows that there is a one-to-one correspondence between $c$ and $S_T \in [S_B, \bar{S}]$. Writing $c = c(S_T)$, we have the following properties for $c(S_T)$:

$$c(S_B) = F'(S_B),\ c(\bar{S}) = F'(\bar{S}),\ \text{and}\ \frac{dc}{dS_T} > 0 \text{ for } S \in [S_B, \bar{S}].$$

Returning to Equation (35), we note that $\gamma = S_B$ is the trivial solution. Properties (37) and (38) imply the existence of a second nontrivial and increasing solution $\gamma = \gamma(\alpha)$ for $\alpha \geq S_B$. It satisfies the following properties.

**Proposition 1.** *Assume either (39) or $S_B \in (\underline{S}, S_o)$. Let $\gamma$ be the increasing (unique) solution of (35). Then it is defined in the interval $[S_B, S_*]$ where $S_* \in (\tilde{S}, \bar{S})$ is such that $\gamma(S_*) = \beta(S_*) =: S^*$. Furthermore, $\gamma(S_B) = S_B$, $\gamma(\alpha) > \alpha$ for $\alpha > S_B$ and $\gamma(\alpha) < \beta(\alpha)$ for $\alpha < S_*$ in the common domain of definition of $\beta$ and $\gamma$ (see Figure 6).*

Observe that, if (39) holds, then a third solution $\gamma = \bar{\gamma}$ exists for $\tilde{S} < \alpha < S_*$. It decreases in $\alpha$ with $\bar{\gamma}(\tilde{S}) = 1$ and $\bar{\gamma}(S_*) = S^*$. The solutions (35) and the function $\beta(\alpha)$ are sketched in Figure 6.

*Remark* 4. For simplicity, we assume (39) for the remaining discussion. This guarantees the existence of a $(S_*, S^*)$ pair. The methods presented in this paper can also be applied to analyze the case when $\beta(\alpha)$ and $\gamma(\alpha)$ are not intersecting. The results are briefly discussed in Section 3.2.

Next we turn to system (TW) where, for the time being, we take

$$S_B < S_T \leq \bar{S}. \tag{40}$$

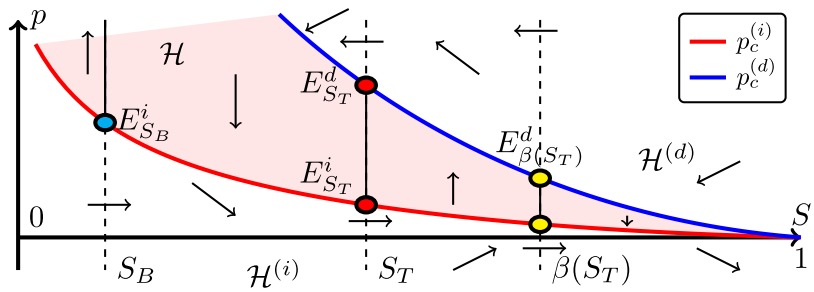


**FIGURE 7** The $S-p$ phase plane and the direction of orbits for Scenario A with $\tilde{S} \le S_T \le \bar{S}$. The regions $\mathcal{H}$, $\mathcal{H}^{(i)}$, $\mathcal{H}^{(d)}$ and the equilibrium lines are marked

Since (TW) is autonomous, it is convenient to represent solutions as orbits in the $(S, p)$-plane, or rather, in the strip $\{(S, p) : 0 \le S \le 1,\ p \in \mathbb{R}\}$. Moreover, orbits are same for any shift in the independent variable $\xi$. Therefore, we may set without loss of generality (see Refs. 9, 45),

$$S(0) = \frac{1}{2}(S_B + S_T). \tag{41}$$

Equilibrium points of (TW) that are of particular interest are

$$E^j_K \equiv (K, p_c^{(j)}(K)), \text{ where } K \in \{S_B, S_T\} \text{ and } j \in \{i, d\}.$$

If $\tilde{S} \le S_T < \bar{S}$, a third pair exists for $K = \beta(S_T)$. The points $E^j_K$ and the direction of the orbits are indicated in Figure 7. By the special nature of the function $\mathcal{F}$, we have in fact that all points of the segments $\overline{E^i_K E^d_K}$ are equilibrium points. Boundary conditions (28) are satisfied if an orbit connects the segments $\overline{E^i_{S_B} E^d_{S_B}}$ and $\overline{E^i_{S_T} E^d_{S_T}}$. As shown in Ref. 45, an orbit can leave $\overline{E^i_{S_B} E^i_{S_B}}$ only from the lowest point $E^i_{S_B}$. Then it enters region $\mathcal{H}^{(i)}$ where it moves monotonically with respect to $S$ as a consequence of the sign in the right-hand side of Equation (31): if $p < p_c^{(i)}(S)$ we have $S' > 0$.

Due to this monotonicity, one can alternatively describe an orbit leaving $E^i_{S_B}$ as a function of the saturation as long as it belongs to $\mathcal{H}^{(i)}$. For given $\tau > 0$ and $S_T$ satisfying (40), let $w(S) = w(S; \tau, S_T)$ denote this function. Then

$$w(S_B; \tau, S_T) = p_c^{(i)}(S_B) \tag{42a}$$

$$\text{and } w(S; \tau, S_T) < p_c^{(i)}(S) \text{ in a right neighborhood of } S_B. \tag{42b}$$

As in Refs. 9, 45, we deduce from (TW) that $w$ should satisfy

$$w'(S; \tau, S_T) = \frac{c\tau \mathcal{G}(S; S_B, S_T)}{p_c^{(i)}(S) - w(S; \tau, S_T)} \text{ for } S > S_B. \tag{43}$$

Using techniques from,[9,45] one can show that initial value problem (43), (42a) has a unique local solution $w(S; \tau, S_T)$ that satisfies (42b).

*Remark* 5. Conversely one recovers the orbit $(S(\xi), p(\xi))$ by substituting $w$ into (31). Using (41) this gives

$$\xi = c\tau \int_{\frac{1}{2}(S_B+S_T)}^{S(\xi)} \frac{d\varrho}{p_c^{(i)}(\varrho) - w(\varrho;\tau,S_T)} d\varrho \text{ and } p(\xi) = w(S(\xi);\tau,S_T).$$

Rewriting (43) as

$$\big(p_c^{(i)} - w\big)\big(w - p_c^{(i)}\big)' + \big(p_c^{(i)} - w\big)p_c^{(i)\prime} = c\tau\mathcal{G}(S;S_B,S_T),$$

we find recalling (P1) that

$$\big((p_c^{(i)} - w)^2\big)' = 2\big(p_c^{(i)} - w\big)p_c^{(i)\prime} - 2c\tau\mathcal{G}(S;S_B,S_T) \le -2c\tau\mathcal{G}(S;S_B,S_T) \text{ in } \big\{w < p_c^{(i)}\big\}. \tag{44}$$

Integrating this inequality from $S_B$ to $S$ gives the lower bound

$$\left.\begin{array}{c} w(S;\tau,S_T) > p_c^{(i)}(S) - \sqrt{2c\tau\Phi(S)} \text{ in } \left\{ w < p_c^{(i)} \right\}, \\ \text{where } \Phi(S) = \Phi(S;S_B,S_T) := -\int_{S_B}^{S} \mathcal{G}(\varrho;S_B,S_T)d\varrho. \end{array}\right\} \tag{45}$$

With $S_T$ satisfying (40), properties (37)-(39) and Proposition 1 imply

$$\left.\begin{array}{c} \Phi(S) > 0 \text{ for } S_B < S < \gamma(S_T) \\ \Phi(S_B) = \Phi(\gamma(S_T)) = 0 \end{array}\right\} \text{ when } S_B < S_T \le S_*, \tag{46a}$$

$$\text{and} \quad \left.\begin{array}{c} \Phi(S) > 0 \text{ for } S_B < S < 1 \\ \lim\limits_{S\nearrow 1} \Phi(S) = +\infty \end{array}\right\} \text{ when } S_* < S_T \le \bar{S}. \tag{46b}$$

Observe that, depending on $S_B$, $S_T$, and $\tau$, the interval where $w(S) < p_c^{(i)}(S)$ is either $(S_B, 1]$ if $w(S)$ and $p_c^{(i)}(S)$ do not intersect, or $(S_B, S_i)$ with $S_i \le 1$ in case there is an intersection at $S = S_i$. In the latter case, it follows immediately from (44) that we must have,

**Proposition 2.** *Suppose there exists $S_i \in (S_B, 1)$ such that $w(S) < p_c^{(i)}(S)$ for $S_B < S < S_i$ and $w(S_i) = p_c^{(i)}(S_i)$. Then $\mathcal{G}(S_i;S_B,S_T) \ge 0$.*

Hence, if the orbit exits through the capillary pressure curve $p_c^{(i)}$, it can only do so at points where $\mathcal{G} \ge 0$. From the discussion above, one defines

$$S_m(\tau,S_T) = \sup\{S \in (S_B,1) \,:\, w(\varrho;\tau,S_T) < p_c^{(i)}(\varrho) \text{ for all } S_B < \varrho < S\}, \tag{47}$$

which is the upper limit of the interval on which $w$ exists. Then we have

**Proposition 3.**

*(a) If $S_B < S_T \le S_*$, then $S_T \le S_m(\tau,S_T) < \gamma(S_T)$ for all $\tau > 0$;*

*(b) If $S_* < S_T \le \bar{S}$ and $w(\beta(S_T);\tau,S_T) < p_c^{(i)}(\beta(S_T))$, then $S_m(\tau,S_T) = 1$ and $\lim\limits_{S\nearrow 1} w(S) = -\infty$.*

In Figure 8, we sketch the behavior of $w(S;\tau,S_T)$ in $\mathcal{H}^{(i)}$. The existence of orbits as in Figure 8 (left) is a direct consequence of the behavior of the lower bound (45). Orbits as in Figure 8 (right) need

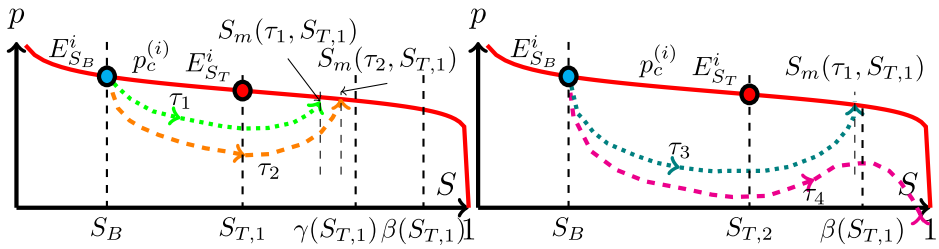


**FIGURE 8** Sketch of orbits represented by $w(S;\tau,S_T)$. (Left) $S_{T,1} \in (S_B, S_*]$, $\tau_1 < \tau_2$; (Right) $S_{T,2} \in (S_*, \bar{S}]$, $\tau_3 < \tau_4$

more attention since the case $S_m(\tau, S_T) < \beta(S_T)$, represented by $\tau_3$, remains to be discussed. We make the behavior as sketched in Figure 8 (right) precise in a number of steps.

Next, we give a general monotonicity result.

**Proposition 4** (Monotonicity)**.**

*(a) For a fixed $S_T \in (S_B, \bar{S}]$ and any pair $0 < \tau_1 < \tau_2$,*

$$w(\cdot;\tau_2,S_T) < w(\cdot;\tau_1,S_T) \text{ in } \{w(\cdot;\tau_1,S_T) < p_c^{(i)}(\cdot)\}$$

*and*

$$S_m(\tau_1,S_T) < S_m(\tau_2,S_T) \text{ if } S_T < S_m(\tau_2,S_T) \le \beta(S_T);$$

*(b) For fixed $\tau > 0$ and any pair $S_B < S_{T,1} < S_{T,2} \le \bar{S}$,*

$$w(\cdot;\tau,S_{T,2}) < w(\cdot;\tau,S_{T,1}) \text{ in } \{w(\cdot;\tau,S_{T,1}) < p_c^{(i)}(\cdot)\}$$

*and*

$$S_m(\tau,S_{T,1}) < S_m(\tau,S_{T,2}) \text{ if } S_{T,2} \le S_m(\tau,S_{T,2}) \le \beta(S_{T,2}).$$

*Remark* 6. To complement Proposition 4, we further state that

$$S_m(\tau_1,S_T) = S_T \quad \text{if} \quad S_m(\tau_2,S_T) = S_T \quad \text{and} \quad S_m(\tau_2,S_T) = 1 \text{ if } S_m(\tau_1,S_T) = 1.$$

The statements follow directly from the ordering of the orbits.

So far we have shown monotonicity of the orbits in $\mathcal{H}^{(i)}$. The next results give the continuous dependence on the parameter $\tau$ and $S_T$. This is addressed in the following results.

**Proposition 5** (Continuous dependence of $w$)**.** *Let $v = p_c^{(i)} - w$. In the context of Figure 4 and with $\Phi$ defined in (45), we have*

*(a) $0 < v^2(S;\tau_2,S_T) - v^2(S;\tau_1,S_T) < 2c(\tau_2-\tau_1)\Phi(S)$ for $S_B < S \le S_m(\tau_1,S_T)$;*

*(b) $0 < v^2(S;\tau,S_{T,2}) - v^2(S;\tau,S_{T,1}) < 2(c(S_{T,2})\,\Phi(S;S_B,S_{T,2}) - c(S_{T,1})\,\Phi(S;S_B,S_{T,1}))$ for $S_B < S \le S_m(\tau,S_{T,1})$;*

**Corollary 1** (Continuous dependence of $S_m$)**.** *Let $\tau_0 > 0$ and $S_{T_0}$ be fixed such that $S_m(\tau_0,S_{T_0}) \le \beta(S_{T_0})$. Then for any small $\varepsilon > 0$, there exists $\delta = \delta(\varepsilon;\tau_0,S_{T_0})$ so that $|S_m(\tau,S_T) - S_m(\tau_0,S_{T_0})| < \varepsilon$ if $\max\{|\tau-\tau_0|, |S_T - S_{T_0}|\} < \delta$ and $S_m(\tau,S_T) < \beta(S_T)$.*

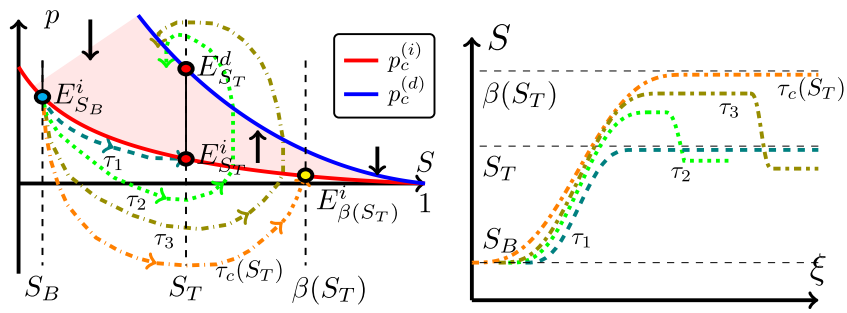


**FIGURE 9** (Left) Ordering of the orbits in the $S$-$p$ phase plane for $S_* < S_T < \bar{S}$ and typical values of $\tau$: $0 < \tau_1 < \tau_2 < \tau_3 < \tau_c(S_T)$. (Right) The behavior of the orbits in the $\xi$-$S$ plane for the same $\tau$ values

Now we are in a position to describe how $S_m$ behaves for different combinations of $S_T$ and $\tau$.

**Proposition 6.** *For each $S_T \in (S_B, \bar{S}]$, there exists a $\tau_m(S_T) > 0$ such that*

$$S_m(\tau, S_T) = S_T \text{ for all } 0 < \tau \le \tau_m(S_T) \text{ and } S_m(\tau, S_T) > S_T \text{ for all } \tau > \tau_m(S_T).$$

The proof of this result is given in proposition 2.1 of Ref. 45. For later purposes, we introduce here some definitions that are related to Proposition 6. Let $\underline{P} = \min_{S\in(S_B,\bar{S})}\{-p_c^{(i)\prime}(S)\} > 0$ and $m_0(S_T) = \sup_{S\in[S_B,S_T]} \mathcal{G}'(S; S_B, S_T) < \infty$, and define

$$\bar{\tau}_m = \frac{\underline{P}^2}{4cm_0(S_T)} \quad \text{and} \quad r_m = \frac{\underline{P}}{2}\left[1 - \sqrt{1 - \frac{\tau}{\bar{\tau}_m}}\right]. \tag{48}$$

Then,

$$p_c^{(i)}(S) + r_m(S - S_T) < w(S; \tau, S_T) < p_c^{(i)}(S) \text{ for all } S \in (S_B, S_T) \text{ and } \tau < \bar{\tau}_m,$$

which directly gives $S_m(S_T, \tau) = S_T$. Thus, $\tau_m > 0$ is defined as

$$\tau_m(S_T) := \sup\{\tau : S_m(S_T, \tau) = S_T\} \ge \bar{\tau}_m > 0. \tag{49}$$

Finally, using [Ref. 9, proposition 4.2(b)] one concludes that $\tau_m(S_T) < \infty$.

We consider now the case $\tau > \tau_m(S_T)$. Propositio-n 3 guarantees that $S_m(S_T, \tau) < \gamma(S_T) \le \beta(S_T)$ if $S_B < S_T \le S_*$. However, for $S_T > S_*$ it is unclear whether $S_m(S_T, \tau)$ is bounded by $\beta(S_T)$ or not. We show below that a $\tau_c = \tau_c(S_T)$ exists in this case such that $S_m(S_T, \tau) \in (S_T, \beta(S_T))$ if $\tau \in (\tau_m(S_T), \tau_c(S_T))$ and $S_m(S_T, \tau_c(S_T)) = \beta(S_T)$ implying from Proposition 3 that $S_m(S_T, \tau) = 1$ for all $\tau > \tau_c(S_T)$ (see Figure 9).

**Proposition 7.** *We have*

*(a) For each $S_T \in (S_*, \bar{S})$, there exists a unique $\tau_c = \tau_c(S_T)$ such that*

$$S_m(\tau_c, S_T) = \beta(S_T).$$

*(b) The function $\tau_c(\cdot)$ is strictly decreasing and continuous on $[S_*, \bar{S}]$. One has $\tau_c(S_T) \to \infty$ as $S_T \searrow S_*$ and $\tau_c(\bar{S}) = \bar{\tau} = \tau_m(\bar{S}) > 0$.*

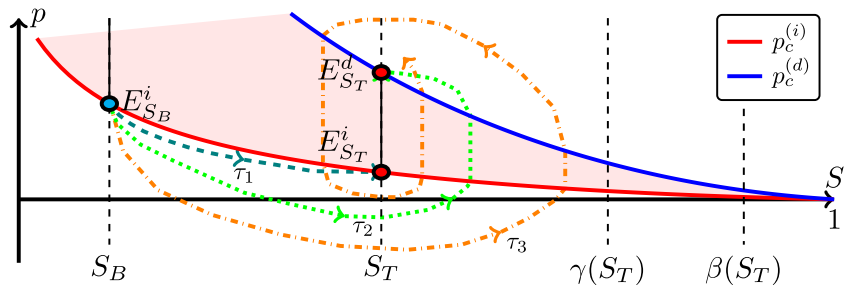


**FIGURE 10** The different cases of $S_B < S_T < S_*$. The orbits are plotted for $0 < \tau_1 < \tau_i < \tau_2 < \tau_d < \tau_3$

After these preliminary statements, we are now in a position to consider the solvability of (TW) for different ranges of $S_T$.

## 3.2 | Problem (TW) with $S_B < S_T \leq \bar{S}$

We investigate the existence of an orbit connecting $(S_B, p_c^{(i)}(S_B))$ and the segment $\overline{E^i_{S_T} E^d_{S_T}}$. Defining

$$\tau_j = \frac{\left(p_c^{(j)\prime}(S_T)\right)^2}{4c\mathcal{G}'(S_T; S_B, S_T)} > 0, \quad j \in \{i, d\}, \tag{50}$$

the eigenvalues of the (TW) system associated with the equilibrium points $E^j_{S_T}$, $j \in \{i, d\}$ are

$$\lambda^j_{\pm} = \frac{p^{(j)\prime}(S_T)}{2c\tau}\left[1 \pm \sqrt{1 - \frac{\tau}{\tau_j}}\right] \text{ implying } \begin{cases} E^j_{S_T} \text{ is stable sink for } \tau \leq \tau_j, \\ E^j_{S_T} \text{ is stable spiral sink for } \tau > \tau_j. \end{cases}$$

This immediately gives $\tau_i \geq \tau_m$ as no monotone orbit can connect with $E^i_{S_T}$ for $\tau > \tau_i$. The general behavior of the orbits for $S_T \in (S_B, S_*]$ are stated in

**Theorem 1.** *Under the assumptions of Scenario A, consider $S_B$ satisfying (33), $S_T \in (S_B, S_*]$ and $\tau_i < \tau_d$. Let $(S, p)$ be the orbit originating from $(S_B, p_c^{(i)}(S_B))$ satisfying (TW). Then, with reference to Figure 10, as $\xi \to \infty$ one gets*

*(a) If $0 < \tau \leq \tau_i$, then either $S \to S_T$ and $p \to p_c^{(i)}(S_T)$ monotonically with respect to $\xi$ through $\mathcal{H}^{(i)}$ (when $\tau \leq \tau_m$) or the orbit $(S, p)$ goes around $\overline{E^i_{S_T} E^d_{S_T}}$ finitely many times and ends up in either $E^i_{S_T}$ or $E^d_{S_T}$ (when $\tau_m < \tau \leq \tau_i$).*

*(b) If $\tau_i < \tau \leq \tau_d$, $(S, p) \to E^d_{S_T}$ after finitely many turns around $\overline{E^i_{S_T} E^d_{S_T}}$.*

*(c) If $\tau_d < \tau$, then $(S, p)$ revolves infinitely many times around $\overline{E^i_{S_T} E^d_{S_T}}$ while approaching it and (28) is satisfied.*

These statements are demonstrated by arguments from [Ref. 45, theorem 2.1 and lemmas 2.1 & 2.2]. We omit the details here. In Theorem 1, we have taken $\tau_i < \tau_d$ without loss of generality. In the $\tau_i > \tau_d$ case, the roles of the equilibrium points $E^i_{S_T}$ and $E^d_{S_T}$ are reversed. The typical behavior of the $S$ and the $p$ profiles with respect to $\xi$ is given in Figure 11. Both $S$ and $p$ are monotone for $\tau < \tau_i$, whereas for $\tau_i < \tau < \tau_d$ they have finite number of local extrema and $p(+\infty) = p_c^{(d)}(S_T)$. For $\tau > \tau_d$,

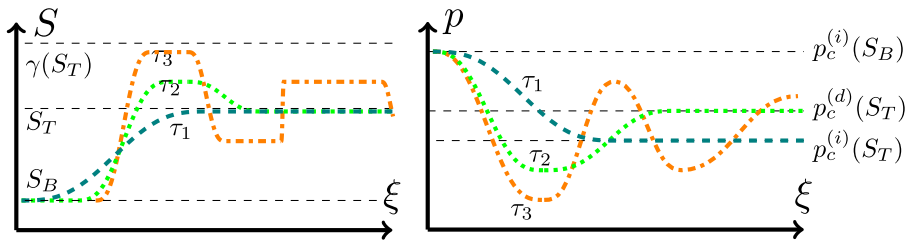


**FIGURE 11** Typical behavior of $S(\xi)$ (left) and $p(\xi)$ (right) for different values of $\tau$. Here profiles for three different $\tau$ values are plotted satisfying $0 < \tau_1 < \tau_i < \tau_2 < \tau_d < \tau_3$. The $\xi = 0$ coordinate is fixed by (41)

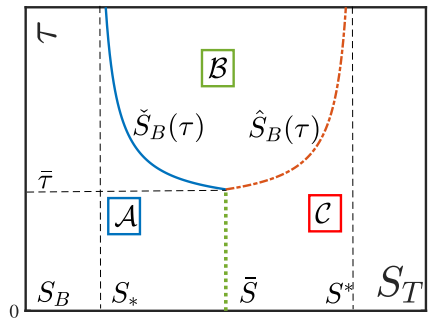


**FIGURE 12** The sets $\mathcal{A}$, $\mathcal{B}$, and $\mathcal{C}$ and the functions $\check{S}_B(\tau)$, $\hat{S}_B(\tau)$

$S$ has infinitely many decaying local extrema, whereas $p$ has no limit. In particular, each $S$ maximum corresponds to a saturation overshoot. On the other hand, the oscillations in $p$ become wider, in line with the assumption $\lim_{\xi\to\infty} p'(\xi) = 0$. In this case, the segment $\overline{E^i_{S_T} E^d_{S_T}}$ becomes an $\omega$-limit set of the orbit.

Turning to the case, $S_T \in (S_*, \bar{S})$, we define the two functions which will be used extensively below.

**Definition 1.** The functions $\hat{S}_B$, $\check{S}_B : [0,\infty) \to (0,1]$ are such that

$$\check{S}_B(\tau) = \begin{cases} (\tau_c)^{-1}(\tau) & \text{for } \tau > \bar{\tau}, \\ \bar{S} & \text{for } 0 \le \tau \le \bar{\tau}, \end{cases} \quad \text{and} \quad \hat{S}_B(\tau) = \beta(\check{S}_B(\tau)).$$

Observe that $\check{S}_B(\tau)$ is a strictly decreasing function whereas $\hat{S}_B(\tau)$ is a strictly increasing function for $\tau > \bar{\tau}$ and $\hat{S}_B(\tau) = \check{S}_B(\tau) = \bar{S}$ for $\tau \le \bar{\tau}$. This is sketched in Figure 12. Numerically computed $\check{S}_B(\tau)$ and $\hat{S}_B(\tau)$ functions are shown in Figure 20.

*Remark* 7. The case when $\beta(\alpha)$ does not intersect $\gamma(\alpha)$ is treated in a similar way. However, since orbits may intersect the line segment $\{S = 1, p \le 0\}$ in this case, a multivalued extension of $p_c^{(i)}$ at $S = 1$ needs to be introduced, see Refs. 9, 45 for further details. With this, one shows that the function $\tau_c(S_T)$ is well-defined in $[\tilde{S}, \bar{S}]$. Then, a $\tau_{_B} > 0$ exists such that $\check{S}_B(\tau_{_B}) = \tilde{S}$ and $\hat{S}_B(\tau_{_B}) = 1$. The subsequent results remain valid if $\hat{S}_B$ and $\check{S}_B$ are extended by

$$\check{S}_B(\tau_{_B}) = \tilde{S} \text{ for } \tau > \tau_{_B}, \quad \text{and} \quad \hat{S}_B(\tau) = 1 \text{ for } \tau > \tau_{_B}.$$

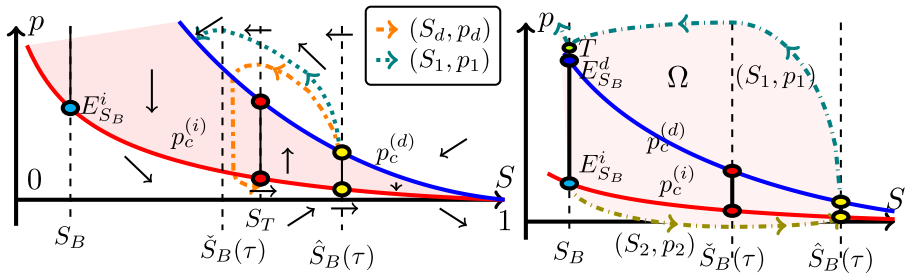


**FIGURE 13** (Left) The direction of orbits for the system (31), (52) and the orbits $(S_d, p_d)$ and $(S_1, p_1)$. Here the orbit $(S_d, p_d)$ connects $E^d_{\hat{S}_B(\tau)}$ and $E^i_{S_T}$. (Right) The domain Ω used in the divergence argument for the hypothetical case where $(S_1, p_1)$ crosses the line $S = S_B$

With this in mind, we define the following sets:

$$\begin{aligned}
\mathcal{A} &= \{(S_T, \tau) : S_B < S_T < \bar{S},\ \tau < \tau_c(S_T)\},\\
\mathcal{B} &= \{(S_T, \tau) : \tau > \bar{\tau},\ \check{S}_B(\tau) < S_T < \hat{S}_B(\tau)\},\\
\mathcal{C} &= \{(S_T, \tau) : \bar{S} < S < S^*,\ \tau < \tau_c(\beta^{-1}(S_T))\}.
\end{aligned} \tag{51}$$

Observe that if $S_T < \bar{S}$ then only regions $\mathcal{A}$ and $\mathcal{B}$ are relevant. With $S_o$ defined in (A1), for $(S_T, \tau) \in \mathcal{A}$ one has

**Proposition 8.** *For a fixed $S_B \in (0, S_o)$ and $(S_T, \tau) \in \mathcal{A}$, the orbit $(S, p)$ entering $\mathcal{H}^{(i)}$ from $E^i_{S_B}$ behaves according to statements (a),(b), and (c) of Theorem 1.*

We discuss the remaining situations, $(S_T, \tau) \in \mathcal{B}$ and $(S_T, \tau) \in \mathcal{C}$ in the next section.

## 3.3 | $(S_T, \tau) \notin \mathcal{A}$

Since $S_T > \check{S}_B(\tau)$, a TW cannot connect $S_B$ and $S_T$. However, a different class of waves is possible when $(S_T, \tau) \in \mathcal{B}$.

**Proposition 9.** *For a fixed $S_B \in (0, S_o)$ and $(S_T, \tau) \in \mathcal{B}$, consider the system*

$$\begin{cases} S' = \frac{1}{c_d \tau}\mathcal{F}(S, p), \\ p' = \mathcal{G}(S; \hat{S}_B(\tau), S_T), \end{cases} \quad \text{with} \quad c_d = \frac{F(\hat{S}_B(\tau)) - F(S_T)}{\hat{S}_B(\tau) - S_T}. \tag{52}$$

*For this system, an orbit $(S_d, p_d)$ exists that connects $E^d_{\hat{S}_B(\tau)}$ for $\xi \to -\infty$ to $\overline{E^i_{S_T} E^d_{S_T}}$ for $\xi \to \infty$.*

*Proof.* Upon inspection of the eigendirections for the system (52) around the equilibrium point $E^d_{\hat{S}_B(\tau)}$ one concludes that there is indeed an orbit $(S_d, p_d)$ that connects to $E^d_{\hat{S}_B(\tau)}$ as $\xi \to -\infty$ from the set $\mathcal{H}^{(d)}$ defined in (15). Moreover, from the direction of the orbits in this case, as shown in Figure 13 (left), it is apparent that after leaving $E^d_{\hat{S}_B(\tau)}$, $S_d$ decreases monotonically till the orbit either hits the curve $p = p_c^{(d)}(S)$ for some $S \le S_T$ or exits $\{S > S_B\}$ through the line $S = S_B$. We prove that it is not possible for the orbit to escape through $S = S_B$. To show this, consider the orbit $(S_1, p_1)$ that satisfies the original (TW) equations and enters $\mathcal{H}^{(d)}$ from $E^d_{\hat{S}_B(\tau)}$. We show that this orbit cannot cross the line $S = S_B$.

The divergence argument presented in Refs. 9, 42, 45 is used for this purpose. To elaborate, assume that $(S_1, p_1)$ intersects the line $S = S_B$ at $T$. Consider the region $\Omega$, enclosed by the segments $\overline{E^i_{S_B} T}$, $\overline{E^i_{\hat{S}_B(\tau)} E^d_{\hat{S}_B(\tau)}}$, the orbit $(S_1, p_1)$ and the orbit $(S_2, p_2)$ that satisfies (TW) and connects $E^i_{S_B}$ to $E^i_{\hat{S}_B(\tau)}$ (see Figure 13 (right)). Introducing the vector-valued function $\vec{R}(S, p) = (\frac{1}{c\tau}\mathcal{F}(S, p), \mathcal{G}(S; S_B, S_T))$ and deduces from (16),

$$\mathrm{div}\vec{R} = \frac{1}{c\tau}\frac{\partial \mathcal{F}}{\partial S}(S, p) = \frac{1}{c\tau}\begin{cases} {p_c^{(i)}}'(S) & \text{in } \mathcal{H}^{(i)}, \\ 0 & \text{in } \mathcal{H}, \\ {p_c^{(d)}}'(S) & \text{in } \mathcal{H}^{(d)}. \end{cases}$$

This gives a contradiction when the divergence theorem is applied to $\vec{R}$ in the domain $\Omega$: the integral of $\vec{R}$ over $\partial\Omega$ is nonnegative whereas $\int_\Omega \mathrm{div}\vec{R} < 0$ from (P1) and Figure 13 (right). Hence, the orbit $(S_1, p_1)$ intersects $p_c^{(d)}(S)$ at some $S \in (S_B, \check{S}_B(\tau)]$.

The wave-speed corresponding to the orbit $(S_d, p_d)$ satisfies

$$c_d < \frac{F(\hat{S}_B(\tau)) - F(S_B)}{\hat{S}_B(\tau) - S_B} = c_i, \tag{53}$$

$c_i$ being the speed of both $(S_1, p_1)$ and $(S_2, p_2)$ waves. Hence, by the continuity of the orbits with respect to $c$, as shown in Proposition 4, it is evident that $(S_d, p_d)$ intersects $p_c^{(d)}(S)$ for some $S_d > S_B$. From here, the rest of the proof is identical to the proof of Theorem 1, and follows the arguments in [Ref. 45, theorem 2.1 and lemmas 2.1 & 2.2]. ■

The general picture is described in the following corollary:

**Corollary 2.** *For $\tau$ small enough, the orbit $(S_d, p_d)$ goes monotonically to $E^d_{S_T}$. For $\tau$ large enough, $(S_d, p_d)$ goes infinitely many times around $\overline{E^i_{S_T} E^d_{S_T}}$ while approaching it, and $\lim_{\xi\to\pm\infty} p_d'(\xi) = 0$.*

Observe that, if $(S_T, \tau) \in \mathcal{C}$ then TWs do not exist between $S_T$ and $\hat{S}_B(\tau)$ since both are in the concave part of $F$ with $S_T > \hat{S}_B(\tau)$. Thus we have exhausted all the possibilities of connecting $S_B$ and $S_T$ with Theorem 1 and Proposition 9.

## 3.4 | Entropy solutions to hyperbolic conservation laws

Under the conditions of Scenario A, we consider the Riemann problem

$$\frac{\partial S}{\partial t} + \frac{\partial F(S)}{\partial z} = 0 \text{ in } \mathbb{R} \times [0, \infty) \tag{54a}$$

$$\text{with } S(z, 0) = \begin{cases} S_T & \text{for } z < 0, \\ S_B & \text{for } z > 0. \end{cases} \tag{54b}$$

In the context of the viscous model discussed in this paper, we consider the Buckley-Leverett Equation (54a) as the limit of System (25) for $N_c \searrow 0$. As a consequence, we only take into account those shock solutions of (54a) that have a viscous profile in the form of a traveling wave satisfying (TW). Such shocks are called admissible because they arise as the $N_c \to 0$ limit of TWs. In this sense, the entropy

condition for shocks satisfying (54a) are equivalent to existence conditions for traveling waves satisfying (TW). This may lead to nonclassical shocks violating the well-known Oleinik entropy conditions, see, for example, Ref. 43.

Here, we assume

$$0 < S_B < S_T < 1, \tag{55}$$

which is more general compared to (33) where the additional constraint of $S_B < S_o$ was imposed. This generalization is possible since $S_B > S_o$ simply implies that the sets $\mathcal{A}$, $\mathcal{B}$ are empty. Our analysis can also be applied to derive the entropy conditions for the case $S_B > S_T$, however, for simplicity we restrict our discussion to (55).

## $(S_T, \tau) \in \mathcal{A}$

As in the usual Buckley-Leverett case (ie, without dynamic capillarity and hysteresis in the regularized models) the solution is given by

$$S(z,t) = \begin{cases} S_T & \text{for } z < ct, \\ S_B & \text{for } z > ct, \end{cases} \text{ where } c = \frac{F(S_T) - F(S_B)}{S_T - S_B}. \tag{56}$$

Here, the shock satisfies the classical Oleinik condition.

## $(S_T, \tau) \in \mathcal{B}$

In this case, the admissible solution is composed of two shocks: an infiltration shock from $S_B$ to $\hat{S}_B(\tau)$, followed by a drainage shock from $\hat{S}_B(\tau)$ to $S_T$.

$$S(z,t) = \begin{cases} S_T & \text{for } z < c_d t, \\ \hat{S}_B(\tau) & \text{for } c_d t < z < c_i t, \\ S_B & \text{for } z > c_i t, \end{cases} \text{ with } \begin{cases} c_i = \dfrac{F(\hat{S}_B(\tau)) - F(S_B)}{\hat{S}_B(\tau) - S_B}, \\ c_d = \dfrac{F(\hat{S}_B(\tau)) - F(S_T)}{\hat{S}_B(\tau) - S_T}. \end{cases} \tag{57}$$

Note that this solution is different from the Oleinik entropy solution.[70] Moreover, the shock connecting $S_B$ and $\hat{S}_B(\tau)$ is undercompressive[71] meaning that it violates the Lax entropy condition. This is because $c_i > F'(\hat{S}_B(\tau))$ for this shock. The trailing shock connecting $\hat{S}_B(\tau)$ to $S_T$ is however classical.

## $(S_T, \tau) \in \mathcal{C}$

The solution in this case violates again the Oleinik entropy condition. It consists of an infiltration shock from $S_B$ to $\hat{S}_B(\tau)$ followed by a rarefaction wave from $\hat{S}_B(\tau)$ to $S_T$,

$$S(z,t) = \begin{cases} S_T & \text{for } z < F'(S_T)t, \\ r(z/t) & \text{for } F'(S_T)t < z < F'(\hat{S}_B(\tau))t, \\ \hat{S}_B(\tau) & \text{for } F'(\hat{S}_B(\tau))t < z < c_i t, \\ S_B & \text{for } z > c_i t, \end{cases} \tag{58}$$

with $r(\cdot)$ satisfying

$$F'(r(\zeta)) = \zeta, \text{ for } F'(S_T) \le \zeta \le F'(\hat{S}_B(\tau)). \tag{59}$$

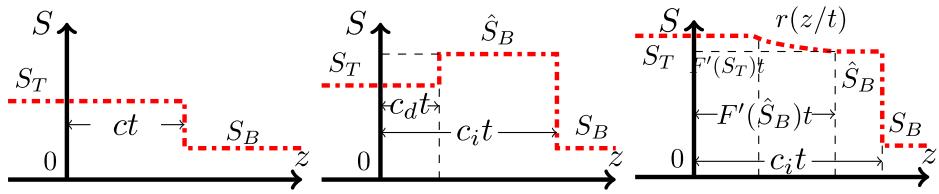


**FIGURE 14** The entropy solutions for (left) $(S_T, \tau) \in \mathcal{A}$, (center) $(S_T, \tau) \in \mathcal{B}$, and (right) $(S_T, \tau) \in \mathcal{C}$. Note that the solutions in the center and the right figures include nonclassical shocks

Since $F$ is concave for $S \in [\hat{S}_B(\tau), S_T]$, $F'$ is monotone implying that $r(\cdot)$ is well-defined. We observe that in the last two cases the solution features a plateau-like region. This plateau appears and grows in time since the speeds of the drainage shock and of the endpoint of the rarefaction wave are lesser than the speed of the infiltration shock. Interestingly, the saturation of the plateau only depends on $p_c^{(i)}$ and not on $p_c^{(d)}$. To be more specific, although the viscous profile consisting of a TW wave connecting $E^d_{\hat{S}_B}$ and $\overline{E^i_{S_T} E^d_{S_T}}$ depends on $p_c^{(d)}$, the shock solution resulting from it, in the hyperbolic limit, does not. However, the role of the drainage curve in the entropy solutions become evident in Scenario B, which is discussed in the next section.

In the absence of hysteresis and for linear higher-order terms, which correspond to constant $k$ and linear $p_c$-$S$ dependence, in [Ref. 43, section 6] it is proved that the nonstandard entropy conditions discussed here are entropy dissipative for the entropy $U(s) = \frac{1}{2}s^2$. However, such an analysis is beyond the scope of this paper. The solution profiles for the Riemann problem are shown in Figure 14.

## 3.5 | Extension to the nonmonotone $F$ case

The analysis so far can be extended to the case where $N_g$ is large resulting in $F$ being nonmonotone. If $S_F \in (0, 1)$ is the saturation where $F(S)$ attains its maximum (see Remark 2 and Figure 3), then the results obtained so far cover the case when $S_T$ and $S^*$ are below $S_F$. However, if $S_T > S_F$ then the TW study has to be conducted also from an $S_T$ perspective, not only from the $S_B$ one. In this scenario, since fronts having negative speeds and thus moving toward $S_T$ become possible, one has to consider the functions $\hat{S}_T(\tau)$, $\check{S}_T(\tau)$ for a fixed $S_T$, similar to $\hat{S}_B(\tau)$, $\check{S}_B(\tau)$ from Definition 1 for fixed $S_B$. Due to the symmetry in the behavior of the fronts approaching $S_B$, respectively, $S_T$, some of the results obtained so far extend straightforwardly to the nonmonotone case. However, a detailed analysis is much more involved and therefore left for future research because of the following two reasons:

1. Depending on the relative positions of $S_B$, $\hat{S}_B$, $S_T$, and $\hat{S}_T$, there are many subcases to consider. In this case, up to three shocks are possible, traveling both forward and backward. Which of these shocks are admissible and how they are connected requires further analysis.
2. For a nonmonotone $F$, when considering the hyperbolic limit in the absence of hysteresis or dynamic effects, the entropy solutions may include rarefaction waves with endpoints moving in opposite directions, forward and backward. When capillary hysteresis is included, preliminary numerical results have provided solutions incorporating two rarefaction waves, one with endpoints traveling backward and another one with endpoints traveling forward, and a stationary shock at $z = 0$. Such solutions still need to be analyzed further.

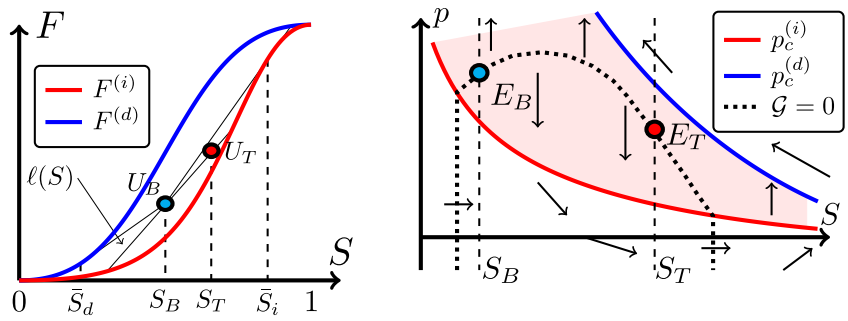


**FIGURE 15** (Left) The graphs of $F^{(i)}$ and $F^{(d)}$, together with the saturations $\bar{S}_i$, $\bar{S}_d$ and the points $U_B$, $U_T$. (Right) The orbit directions for Case (i) for two equilibrium points $E_B$ and $E_T$. The black dotted curve represents points where $\mathcal{G}(S,p) = 0$, implying $p' = 0$

## 4 | HYSTERETIC RELATIVE PERMEABILITIES AND SMALL $N_g$ (SCENARIO B)

For Scenario B, the flux function $F(S,p)$ is composed of $F^{(j)} = f^{(j)} + N_g h^{(j)}$ for $j \in \{i,d\}$ and $\bar{F} = \bar{f} + N_g \bar{h}$ such that

$$F(S,p) = \begin{cases} F^{(d)}(S) & \text{if } (S,p) \in \mathcal{H}^{(d)}, \\ \bar{F}(S,p) & \text{if } (S,p) \in \mathcal{H}, \\ F^{(i)}(S) & \text{if } (S,p) \in \mathcal{H}^{(i)}. \end{cases} \tag{60}$$

It has the following properties

(A2) $F \in C(\mathcal{W})$, $\bar{F} \in C^2(\mathcal{H})$, $\partial_p F > 0$ in $\mathcal{H}$ and $F^{(i)}$, $F^{(d)}$ satisfy properties stated for $F$ in A1. In addition, $F^{(d)}(S) > F^{(i)}(S)$ for $0 < S < 1$.

In this scenario, $S_B$ can be taken in the entire interval (0,1) and $p_B$ can be chosen independently as long as $(S_B, p_B) \in \mathcal{H}$, that is,

$$0 < S_B < 1 \quad \text{and} \quad p_B \in \left[p_c^{(i)}(S_B), p_c^{(d)}(S_B)\right]. \tag{61}$$

This is different from Scenario A where $S_B$ is restricted to the interval $(0, S_o)$ and $p_B$ is fixed to $p_B = p_c^{(i)}(S_B)$.

We first introduce some notation.

**Definition 2.** For $k \in \{B,T\}$ let $E_k = (S_k, p_k)$ and $U_k = (S_k, F(S_k,p_k))$ (see Figure 15 (left)). We define the saturations $\bar{S}_j$, $j \in \{i,d\}$ as the $S$-coordinates of the tangent points to $F^{(j)}(S)$ from $U_B$ such that $\bar{S}_i \geq S_B$ and $\bar{S}_d \leq S_B$.

Observe that the saturations $\bar{S}_j$, for $j \in \{i,d\}$, are functions of $U_B$. The properties of $F^{(j)}$ further ensure that they are well-defined. If $S_B$ is such that $F^{(i)''}(S_B) \leq 0$ and $p_B = p_c^{(i)}(S_B)$ then $\bar{S}_i = S_B$. Similarly if $F^{(d)''}(S_B) \geq 0$ and $p_B = p_c^{(d)}(S_B)$ then $\bar{S}_d = S_B$.

The existence of TWs is analyzed for the following two cases:

$$\text{Case (i): } S_B < S_T \leq \bar{S}_i, \quad \text{and} \quad \text{Case (ii) : } \bar{S}_d \leq S_T < S_B.$$

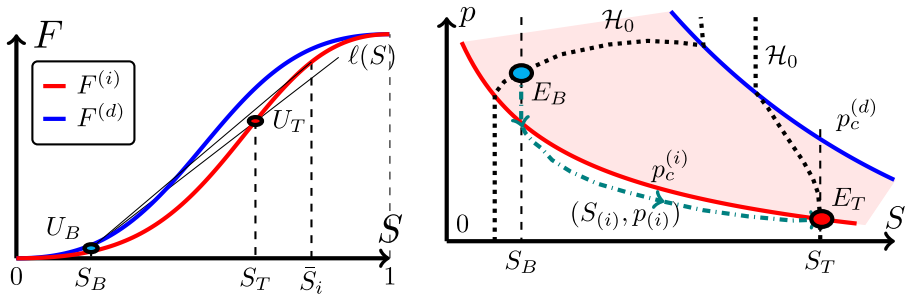


**FIGURE 16** $U_B, U_T, \ell(S)$ used in Proposition 11 in the $S$-$F$ plane. (Right) The $S$-$p$ plane and the orbit $(S_{(i)}, p_{(i)})$ for Case (i) with $F^{(i)}(S_T) > F(S_B, p_B)$ and $\tau < \tau_i^*(S_T)$

Regarding the choice of $p_T$, we have the following.

**Proposition 10.** *Let $S_B$ and $S_T$ be as in Case (i) or Case (ii). Then any solution of (TW) that connects $E_B$ and $E_T$ can only exist if $p_T = p_c^{(i)}(S_T)$ or $p_T = p_c^{(d)}(S_T)$.*

*Proof.* Since $E_T$ is an equilibrium point, $\mathcal{F}(S_T, p_T) = 0$, which implies that $p_T \in [p_c^{(i)}(S_T), p_c^{(d)}(S_T)]$. The directions of the orbits for $p_T$ in this interval are displayed in Figure 15 (right). We proceed by introducing the set

$$\mathcal{H}_0 = \{(S, p) : S \in (0, 1),\ p \in \mathbb{R} \text{ such that } \mathcal{G}(S, p) = 0\}.$$

It corresponds to the black dotted curve in Figure 15 (right). Let $\ell = \ell(S)$, defined in (32), be the line passing through $U_B$ and $U_T$. If $\ell$ intersects $F^{(i)}$ at $S = S_H$, then the vertical half-line $\{(S_H, p) : p < p_c^{(i)}(S_H)\}$ lies in $\mathcal{H}_0$ due to the definition of $F$ in (60). Concerning $F^{(d)}$, $\ell$ has either zero, one or two intersection points (see Figure 16 (left)). In the latter case, as before, $\mathcal{H}_0$ contains one or two vertical half-lines as shown in the (right) plot of Figure 16. However, this aspect plays no major role in the analysis below.

Every point in the set $\mathcal{H}_0 \cap \mathcal{H}$ is an equilibrium point. However, all points in the set $\mathcal{H}_0 \cap \text{int}(\mathcal{H})$ (the interior of $\mathcal{H}$ being referred to as $\text{int}(\mathcal{H})$ here) are unstable and as follows from Figure 15 (right), no orbit can reach these points as $\xi \to \infty$. This eliminates all other possibilities to reach $E_T$ as $\xi \to \infty$ except for $p_T = p_c^{(i)}(S_T)$ and $p_T = p_c^{(d)}(S_T)$. ■

We now consider the two cases separately.

## 4.1 | Case (i): $S_B < S_T \le \bar{S}_i$

The main result of this section is

**Proposition 11.** *Assume (61) and let $S_T \in (S_B, \bar{S}_i]$, $p_T = p_c^{(i)}(S_T)$, and $F^{(i)}(S_T) > F(S_B, p_B)$. Then a $\tau_i^*(S_T) > 0$ exists such that for all $\tau < \tau_i^*(S_T)$ there is an orbit satisfying (TW) and connecting $E_B$ to $E_T$.*

*Proof.* Consider the orbit $(S_{(i)}, p_{(i)})$ that leaves $E_B$ vertically through the half-line $\{S = S_B, p < p_B\}$. The directions of the orbits in $\mathcal{H}$ imply that $(S_{(i)}, p_{(i)})$ intersects $p_c^{(i)}(S)$ and enters $\mathcal{H}^{(i)}$ (the region

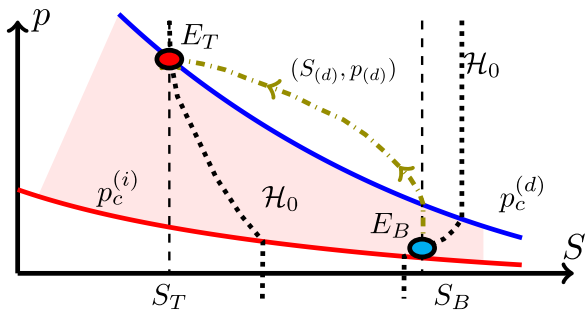


**FIGURE 17** The orbit $(S_{(d)}, p_{(d)})$ for Case (ii) with $F^{(d)}(S_T) < F(S_B, p_B)$ and $\tau < \tau_d^*(S_T)$

under the graph of $p_c^{(i)}$) at some finite $\xi \in \mathbb{R}$ (see Figure 16 (right)). In $\mathcal{H}^{(i)}$, its motion is governed by the system

$$\begin{cases} S_{(i)}' = \frac{1}{c_{(i)}\tau}\Big(p_c^{(i)}(S_{(i)}) - p_{(i)}\Big), \\ p_{(i)}{}' = \mathcal{G}_i(S_{(i)}) := \mathcal{G}\Big(S_{(i)}, p_c^{(i)}(S_{(i)})\Big), \end{cases} \quad \text{with} \quad c_{(i)} = \frac{F^{(i)}(S_T) - F(S_B, p_B)}{S_T - S_B} > 0. \tag{62}$$

Note that $\mathcal{G}_i(S) = (F^{(i)}(S) - \ell(S))/h^{(i)}(S)$. The system (62) has exactly the same structure as (TW) described in Section 3. Defining $\tau_i^*(S_T)$ similar to $\tau_m$ in Proposition 6, the result follows directly. ■

*Remark* 8. Observe that the construction fails if $F^{(i)}(S_T) < F(S_B, p_B)$ which is intuitive since the overall process is not infiltration in this case. If one prescribes a flux $F = F_T$ at $\xi \to \infty$ which is less than $F(S_B, p_B)$, then Propositions 10 and 11 force the saturation at $\xi \to \infty$ to be $S_T = (F^{(d)})^{-1}(F_T) < S_B$, reducing the problem to Case (ii). However, if one fixes the saturation $S_T$ so that $F(S_B, p_B) > F^{(i)}(S_T)$, then we get a frozen profile with a $p_T \in (p_c^{(i)}(S_T), p_c^{(d)}(S_T))$ that satisfies $F(S_T, p_T) = F(S_B, p_B)$. This is explained further in Section 5.2. We set $\tau_i^*(S_T) = \infty$ in this case.

Proposition 11 implies the following:

**Corollary 3.** *Under the assumptions of Proposition 11, let $S_{(i)}(\underline{\xi}) = S$ for some $S \in (S_B, S_T]$ and $\underline{\xi} \in \mathbb{R}$. Define $\underline{w}(S;\tau) := p_{(i)}(\underline{\xi}) < p_c^{(i)}(S)$. Then $\lim_{\tau\to 0} \underline{w}(S;\tau) = p_c^{(i)}(S)$.*

Here, $\underline{w}$ is the counterpart of $w$ defined in Section 3 for Scenario A. The proof of Corollary 3 is based on the inequality (45) which is satisfied in this case by $\underline{w}$. From Corollary 3, one obtains that for Case (i), if $\tau \searrow 0$, meaning that if the dynamic capillarity is vanishing, then the orbit follows either the scanning curve, here the line segment $\{S = S_B, p_c^{(i)}(S_B) < p < p_B\}$, or the infiltration curve $p_c^{(i)}$. The result is analogous to the results for capillary hysteresis given in [Ref. 9, section 3].

## 4.2 | Case (ii): $\bar{S}_d \le S_T < S_B$ and stability of plateaus

The counterpart of Proposition 11 for Case (ii) is (see also Figure 17),

**Proposition 12.** *Assume (61) and let $S_T \in [\bar{S}_d, S_B)$, $p_T = p_c^{(d)}(S_T)$, and $F^{(d)}(S_T) < F(S_B, p_B)$. Then a $\tau_d^*(S_T) > 0$ exists such that for all $\tau < \tau_d^*(S_T)$ there is an orbit $(S_{(d)}, p_{(d)})$ satisfying (TW) and connecting $E_B$ to $E_T$. Moreover, for a fixed $S_{(d)} = S \in [S_T, S_B)$, one has $p_{(d)} \to p_c^{(d)}(S)$ as $\tau \to 0$.*

Finally, we investigate a special case related to the development of stable saturation plateaus in infiltration experiments. For $S_B \in (0, 1)$, and $S_T \in (S_B, 1)$ a stable plateau is formed when an infiltration

wave, from $S_B$ to $S_P \in (S_T, 1)$, followed by a drainage wave, from $S_P$ to $S_T$, both have the same speed resulting in the width of the plateau to remain constant. This is different from the plateaus described in (57) where the speeds of the infiltration and the drainage fronts are necessarily different. The existence of stable saturation plateaus has been widely studied experimentally[29,33,35] and numerically.[15,60] Although results regarding stability of the plateau are available,[15,60] the mechanism behind its development is still not well understood. Here, we give an example where our analysis predicts that such a plateau will develop. Specifically, it occurs when $\tau > \tau_i^*(S_T)$ and a direct monotone orbit from $E_B$ to $(S_T, p_c^{(i)}(S_T))$ is no longer possible. This is verified numerically in Section 5.2.

**Proposition 13.** *Assume (61) and let $S_T \in (S_B, 1)$ be such that the line $\ell$ through $U_B = (S_B, F(S_B, p_B))$ and $U_T = (S_T, F^{(d)}(S_T))$ in the $F$-$S$ plane intersects $F^{(i)}$ at some $S = S_P \in (S_T, \bar{S}_i)$. Consider the system (TW) with the wave-speed*

$$c_P = \frac{F^{(d)}(S_T) - F(S_B, p_B)}{S_T - S_B} = \frac{F^{(i)}(S_P) - F(S_B, p_B)}{S_P - S_B} = \frac{F^{(i)}(S_P) - F^{(d)}(S_T)}{S_P - S_T}.$$

*For this system, let $(S_{(i)}^P, p_{(i)}^P)$ be the orbit that passes through $\mathcal{H}^{(i)}$ and connects to the equilibrium point $(S_B, p_B)$ as $\xi \to -\infty$, described in Proposition 11. Similarly, let $(S_{(d)}^P, p_{(d)}^P)$ be the orbit passing through $\mathcal{H}^{(d)}$ and connecting to $(S_P, p_c^{(i)}(S_P))$ as $\xi \to -\infty$, described in Proposition 12. Assume that $0 < \tau < \max\{\tau_i^*(S_P), \tau_d^*(S_T))\}$ where the $\tau_i^*(S_P)$ and the $\tau_d^*(S_T)$ values correspond to the orbits $(S_{(i)}^P, p_{(i)}^P)$ and $(S_{(d)}^P, p_{(d)}^P)$, respectively. Then, $(S_{(i)}^P, p_{(i)}^P) \to (S_P, p_c^{(i)}(S_P))$ as $\xi \to \infty$ and $(S_{(d)}^P, p_{(d)}^P) \to (S_T, p_c^{(d)}(S_T))$ as $\xi \to \infty$.*

The proof follows directly from Propositions 11 and 12.

## 4.3 | Entropy solutions

We can now discuss the entropy solutions of the Riemann problem (54) under the assumptions of Scenario B. To be more specific, we give a selection criteria for the solutions of the system

$$\begin{cases} \frac{\partial S}{\partial t} + \frac{\partial F(S,p)}{\partial z} = 0, \\ p \in \frac{1}{2}\left(p_c^{(d)}(S) + p_c^{(i)}(S)\right) - \frac{1}{2}\left(p_c^{(d)}(S) - p_c^{(i)}(S)\right) \cdot \operatorname{sign}\left(\frac{\partial S}{\partial t}\right), \end{cases} \quad \text{in } \mathbb{R} \times [0, \infty) \tag{63}$$

$$\text{with } S(z,0) = \begin{cases} S_T & \text{for } z < 0, \\ S_B & \text{for } z > 0, \end{cases} \text{ and } p(z,0) = p_B \text{ for } z > 0. \tag{64}$$

We view (63) as the limit of $(\mathcal{P})$ when the capillary effects vanish. However, hysteresis is still present in the model.

Note that $\tau$ still plays a role in determining the entropy solution despite being absent in (63). This is similar to what we saw in Section 3. However, the focus here being hysteresis in permeability and capillary pressure, for a fixed $S_B \in (0, 1)$ we take

$$0 < \tau < \min\left\{ \inf_{S_T \in (S_B, \bar{S}_i]} \tau_i^*(S_T), \inf_{S_T \in [\bar{S}_d, S_B)} \tau_d^*(S_T) \right\}. \tag{65}$$

Observe that (65) does not provide a void interval for $\tau$. To see this, note that $\tau_i^*(S_T)$ is defined similar to $\tau_m$ in Proposition 6 and thus, it satisfies the inequality in (49), that is, it has the positive quantity $\bar{\tau}_m$

as its lower bound. Although $\bar{\tau}_m$ in Proposition 6 actually depends on $S_T$, one sees from (48) that the values of $\bar{\tau}_m$ are bounded away from 0 uniformly with respect to $S_T$. Hence, $\tau_i^*(S_T)$ is also bounded uniformly away from 0. Similar argument holds for $\tau_d^*(S_T)$.

We now consider the cases $S_T > S_B$ and $S_T < S_B$ separately.

## $S_T > S_B$

If $S_T \le \bar{S}_i$ ($\bar{S}_i$ introduced in Definition 2) and $F^{(i)}(S_T) > F(S_B, p_B)$ then the entropy solution is a shock:

$$S(z,t) = \begin{cases} S_T & \text{for } z < c_{(i)}t, \\ S_B & \text{for } z > c_{(i)}t, \end{cases} \quad \text{with} \quad c_{(i)} = \frac{F^{(i)}(S_T) - F(S_B, p_B)}{S_T - S_B}. \tag{66}$$

For $F^{(i)}(S_T) < F(S_B, p_B)$, from Remark 8, the solution is (66) but with $c_{(i)} = 0$, that is, it is a stationary shock. However, if $S_T > \bar{S}_i$ then the solution becomes more complex, combining a rarefaction wave with a shock:

$$S(z,t) = \begin{cases} S_T & \text{for } z < F^{(i)\prime}(S_T)t, \\ r_{(i)}(z/t) & \text{for } F^{(i)\prime}(S_T)t < z < F^{(i)\prime}(\bar{S}_i)t, \\ \bar{S}_i & \text{for } F^{(i)\prime}(\bar{S}_i)t < z < c_{(i)}t, \\ S_B & \text{for } z > c_{(i)}t. \end{cases} \tag{67}$$

Here, $r_{(i)}(\cdot)$ satisfies

$$F^{(i)\prime}(r_{(i)}(\zeta)) = \zeta, \text{ for } F^{(i)\prime}(S_T) \le \zeta \le F^{(i)\prime}(\bar{S}_i).$$

## $S_T < S_B$

If $S_T \ge \bar{S}_d$ then the entropy solution for $F(S_B, p_B) > F^{(d)}(S_T)$ is the shock

$$S(z,t) = \begin{cases} S_T & \text{for } z < c_{(d)}t, \\ S_B & \text{for } z > c_{(d)}t, \end{cases} \text{with } c_{(d)} = \frac{F(S_B, p_B) - F^{(d)}(S_T)}{S_B - S_T}, \tag{68}$$

and for $F(S_B, p_B) < F^{(d)}(S_T)$ it is (68) with $c_{(d)} = 0$. If $S_T < \bar{S}_d$ then the solution has a similar structure to (67), that is,

$$S(z,t) = \begin{cases} S_T & \text{for } z < F^{(d)\prime}(S_T)t, \\ r_{(d)}(z/t) & \text{for } F^{(d)\prime}(S_T)t < z < F^{(d)\prime}(\bar{S}_d)t, \\ \bar{S}_d & \text{for } F^{(d)\prime}(\bar{S}_d)t < z < c_{(d)}t, \\ S_B & \text{for } z > c_{(d)}t, \end{cases} \tag{69}$$

with the function $r_{(d)}(\cdot)$ satisfying

$$F^{(d)\prime}(r_{(d)}(\zeta)) = \zeta, \text{ for } F^{(d)\prime}(S_T) \le \zeta \le F^{(d)\prime}(\bar{S}_d).$$

## 5 | NUMERICAL RESULTS

For the numerical experiments, we solve $(\tilde{\mathcal{P}})$ (System (26)) in a domain $(z_{in}, z_{out})$, where $z_{in} < 0$ and $z_{out} > 0$. As an initial condition for the saturation variable, we choose a smooth and monotone approximation of the Riemann data:

$$S(z,0) = \begin{cases} S_T \text{ for } z < -l, \\ \frac{(S_B+S_T)}{2} + \frac{(S_T-S_B)}{4l^3} z \cdot (z^2 - 3l^2) \text{ for } -l \le z \le l, \\ S_B \text{ for } z > l. \end{cases} \tag{70}$$

Here, $l$ is a smoothing parameter, $S_T$ denotes the saturation induced by a certain injection rate and $S_B$ is the initial saturation within the porous medium. To model the capillary pressure, a van Genuchten parameterization is considered, that is,

$$p_c^{(j)}(S) = \Lambda_j \left( S^{-\frac{1}{m_j}} - 1 \right)^{1-m_j}, \; j \in \{i, d\}.$$

In the remainder of this section, we use the following parameter set: $\Lambda_i = 3.5$, $m_i = 0.92$, $\Lambda_d = 7$, and $m_d = 0.9$. To solve $(\tilde{\mathcal{P}})$ numerically, for $n \in \mathbb{N} \cup \{0\}$ and $t_0 = 0$, we solve within the time step

$$\left[t_n, t_{n+1}\right] \text{ of width } \Delta t_n = t_{n+1} - t_n,$$

the elliptic problem

$$-\frac{\partial}{\partial z}\left( F(S,p) + h(S,p)\frac{\partial p}{\partial z} \right) = \frac{1}{\tau}\mathcal{F}(S,p),$$

with respect to the pressure variable $p$. For a given $S$, this is a nonlinear elliptic problem and to solve it, a linear iterative scheme is employed which is referred to as the L-scheme in literature[73-75]:

$$L\left(p_n^i - p_n^{i-1}\right) - \frac{\partial}{\partial z}\left( F\left(S_n, p_n^{i-1}\right) + h\left(S_n, p_n^{i-1}\right)\frac{\partial p_n^i}{\partial z} \right) = \frac{1}{\tau}\mathcal{F}\left(S_n, p_n^{i-1}\right).$$

Here, $p_n^i$ denotes the pressure at the $i$th iteration and $p_n^0 = p(z, t_n)$. On closer examination, the L-scheme corresponds to a linearization of the nonlinear problem, since for each iteration a linear equation in the unknown pressure variable $p_n^i$ is solved. For Scenario A the parameter $L$ is set to $L = \frac{1}{\tau}$ to ensure convergence of the L-scheme[45,73] and for Scenario B the modified variant of the L-scheme is used[9,75] to speed up the convergence, since in this scenario the stiffness matrix has to be recomputed in every iteration. A standard cell centered finite volume scheme is considered for discretizing the linearized elliptic problem in space. Having the pressure variable $p_n$ and the saturation variable $S_n$ for $t = t_n$ at hand, we update the saturation as follows:

$$S_{n+1} = S_n + \frac{\Delta t_n}{\tau}\mathcal{F}\left(S_n, p_n\right).$$

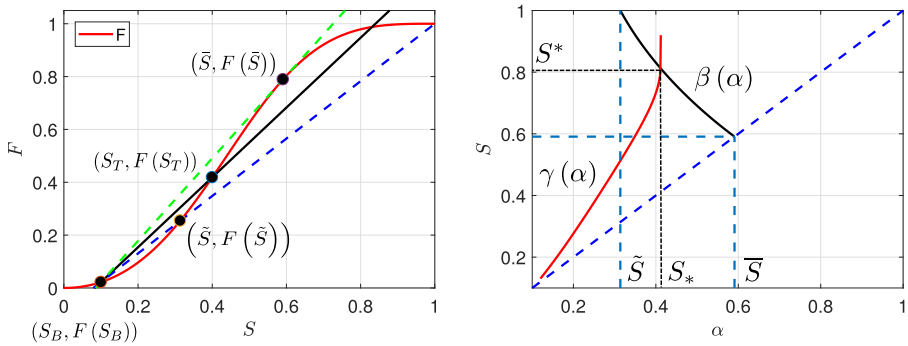


**FIGURE 18** Fractional flow function $F$ for Scenario A (left). The characteristic points $\tilde{S}$, $\bar{S}$, and $S_T$ are shown. (Right) Curves for $\gamma$ (red) and $\beta$ (black) corresponding to $F$. The intersection point of these curves is denoted by $(S_*, S^*)$

## 5.1 | Numerical results for Scenario A

First we illustrate the theoretical findings of Scenario A. The boundary conditions with respect to the pressure variable are of Neumann type at $z = z_{in}$ and of Dirichlet type at $z = z_{out}$:

$$p'(z_{in}, t) = 0 \text{ and } p(z_{out}, t) = p_c^{(i)}(S_B) \text{ for all } t > 0. \tag{71}$$

The boundaries of the domain are given by: $z_{in} = -10$ and $z_{out} = 500$. Because we do not include hysteresis in the relative permeabilites, the flux function $F$ depends only on $S$ and is determined by:

$$f(S) = \frac{S^2}{S^2 + (1-S)^2} \quad \text{and} \quad N_g = 1.$$

The numerical results presented in this subsection are related to $t = t_{\text{end}} = 300$. For the parameters of the initial condition, we take:

$$S_B = 0.1, \quad S_T = 0.4, \quad \text{and} \quad l = 1.$$

Based on these data, some of the variables and constants occurring in Section 3.1, Figures 4 and 6 are computed, that is:

$$\tilde{S} \approx 0.3138, \quad \bar{S} \approx 0.5909, \quad S_o \approx 0.4393, \quad S_* \approx 0.4111, \text{ and } S^* \approx 0.8132. \tag{72}$$

Moreover, the curves for $\gamma$ and $\beta$ are determined (see Figure 18). Observe that, from our choice, $S_B < S_o$ and $S_T \in (S_B, S_*]$. Next, the characteristic $\tau$-values for drainage and imbibition are computed. Using (50) and given parameters, we obtain:

$$\tau_i = 0.0452 \quad \text{and} \quad \tau_d = 0.2620.$$

Because the requirements listed in Theorem 1 are all fulfilled, we can compare the numerical results with the claims contained in the theorem. For this purpose, we choose $\tau$ from the following set:

$$\tau \in \{0.045,\ 0.25,\ 1.0,\ 2.0\},$$

and study the resulting $S$-$p$ orbits. Considering Figure 19, it can be observed that for $\tau < \tau_i$ monotone

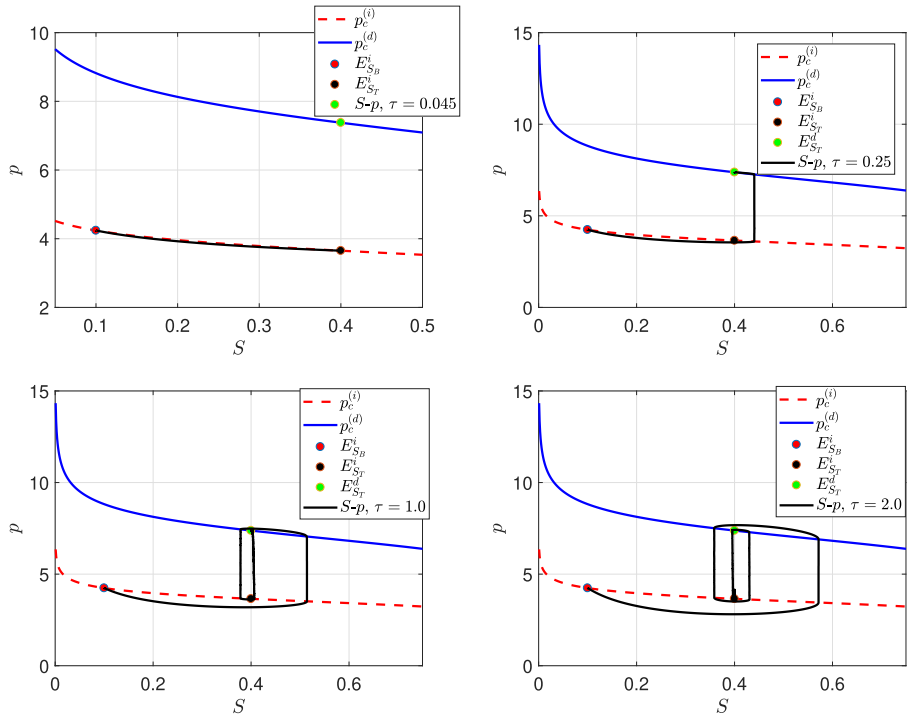


**FIGURE 19** Orbits for different $\tau$ parameters in the $S-p$ plane

saturation waves are produced by the numerical model linking $E^i_{S_B}$ and $E^i_{S_T}$. In the other cases, a saturation overshoot can be detected, where for $\tau_i < \tau < \tau_d$ the orbit ends up at the equilibrium point $E^d_{S_T}$ and for $\tau > \tau_d$ the orbits spiral around the segment $\overline{E^i_{S_T} E^d_{S_T}}$. If we choose larger values of $\tau$, the corresponding $S_m(\tau, S_T)$ value of the orbit increases. This supports the claims of Corollary 1 and Proposition 4. Similar results including variation of saturation with $\xi$ can be found in Ref. 45.

The parameter choice considered so far, corresponds to the solution class $\mathcal{A}$ (see (51)), whose entropy solution consists of a single shock without any saturation overshoots (see Figure 21 (top)). However, there are two further solution classes, $\mathcal{B}$ and $\mathcal{C}$ (see (51)), arising in the context of Scenario A, represented by entropy solutions (57) and (58). In case of solution class $\mathcal{B}$, the entropy solution is given by saturation plateau that is formed by an infiltration wave followed by a drainage wave. The saturation at plateau level is denoted by $\hat{S}_B(\tau)$. For solution class $\mathcal{C}$, the entropy solution exhibits a rarefaction wave connecting $S_T$ with $\hat{S}_B(\tau)$, which is connected to $S_B$ by a shock. To observe these cases numerically, we compute the $\hat{S}_B(\tau)$ and $\check{S}_B(\tau)$ curves introduced in Definition 1 (see Figure 20). In the figure, we fix $\tau = 1$ and vary $S_T$ so that the pairs $(S_T, \tau)$ belong to one of the sets $\mathcal{A}$, $\mathcal{B}$, and $\mathcal{C}$. The results are shown in Figure 21 with the (left) plot showing the variation of $S$ with $z$, and the (right) plot showing the profiles in the $S$-$p$ phase plane. The curves corresponding to Set $\mathcal{A}$ show a direct TW wave connecting $S_B$ and $S_T = 0.35$. Some oscillatory behavior around $S_T$ can be observed since $\tau$ is comparatively large, however, the existence of a single TW between $S_B$ and $S_T$ implies that these states are connectable by an admissible shock in the hyperbolic limit. Next, choosing $S_T = 0.55$, $(S_T, \tau)$ lies in Set $\mathcal{B}$, and a solution consisting of an infiltration wave followed by a drainage wave is computed in accordance with the theory. The development of the plateau is shown in Figure 22. Again, small oscillations are seen in the drainage wave part which is expected from Corollary 2 since $\tau$ is large. The resulting plateau has saturation 0.7158, whereas, the prediction from Figure 20 is $\hat{S}_B(\tau) = 0.7254$.

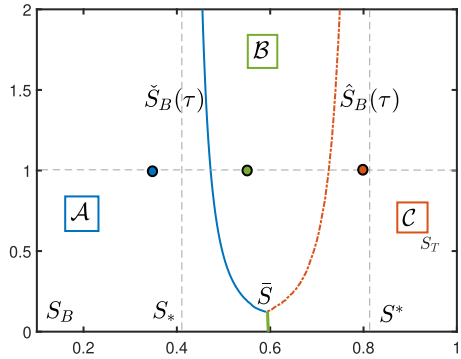


**FIGURE 20** The $\hat{S}_B(\tau)$ and $\check{S}_B(\tau)$ curves computed for $S_B = 0.1$. The characteristic saturations are as in (72). The corresponding Sets $\mathcal{A}$, $\mathcal{B}$, and $\mathcal{C}$ along with $(S_T, \tau)$ test pairs used in Figure 21 are shown

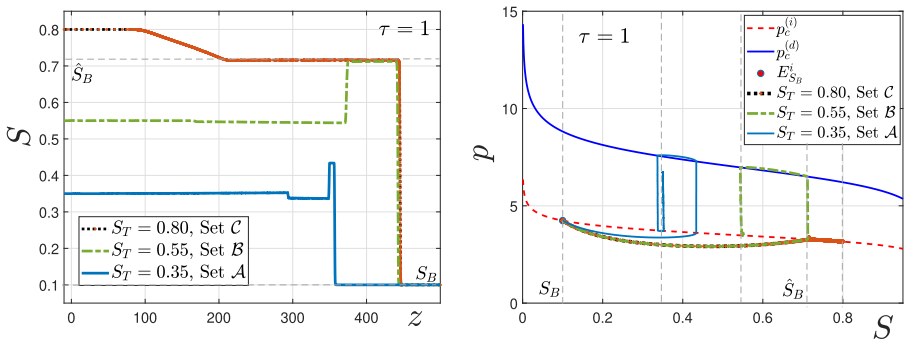


**FIGURE 21** Numerical solutions corresponding to different $(S_T, \tau)$ pairs from solution classes $\mathcal{A}$, $\mathcal{B}$, and $\mathcal{C}$, marked in Figure 20. Here, $\tau = 1$ is fixed and $S_T$ is chosen from $\{0.35, 0.55, 0.8\}$. The (left) plot shows the variation of $S$ with $z$, whereas, the (right) plot shows $p$ versus $S$. The saturation plateau for the Sets $\mathcal{B}$ and $\mathcal{C}$ is observed at $\hat{S}_B = 0.7158$

Finally, for $S_T = 0.8$, the pair $(S_T, \tau)$ belongs to the Set $\mathcal{C}$. The numerical solution exhibits a shock-like structure followed by a plateau and they coincide with the infiltration wave of Set $\mathcal{B}$ on both plots of Figure 21. Moreover, a rarefaction wave between $\hat{S}_B(\tau)$ and $S_T$ is detected. Thus, we conclude that the saturation profiles in Figure 21 correspond to the entropy solutions depicted in Figure 14 and the numerical results are in agreement with the theory.

### 5.1.1 | Stability of the TW profiles

Another important issue with regards to our discussion is the stability of the TW solutions. For the dynamic capillarity model, linearized stability of TW profiles was investigated in Refs. 76, 77 for convex flux functions. The TWs were found to be stable under small perturbations. Linear stability of the steady-state solution for the dynamic capillarity model was shown in Ref. 37. However, such a result might not hold when hysteresis is included. For example, in Ref. 38 it was shown that with hysteresis, stable planar fronts are not guaranteed. Moreover, linearized stability results might not extend to large deviations from the TW profile. Nevertheless, in our case, the stability of the TW profiles is indicated by the numerical computations. More precisely, the numerical examples are presenting the solution profiles for the partial differential equations, thus not for the TW. These numerical results are obtained

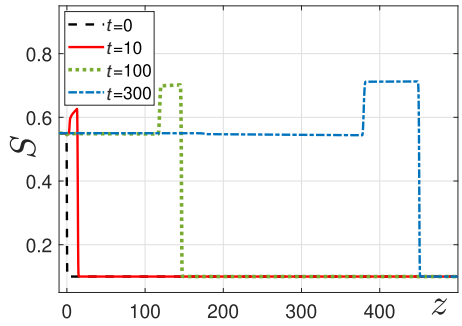


**FIGURE 22** The time evolution of the solution profile for $(S_T, \tau) \in \mathcal{B}$

by using a regularized initial data in (70). The solution quickly develops into profiles that are either an approximation of the corresponding TW if the values of $S_T$ and $S_B$ are states that can be connected by a TW for the chosen parameters, or it exhibits a plateau value that approximates very well the left state that can be connected by a TW to $S_B$. Moreover, this is obtained irrespective of the choice of the regularization parameter $\ell$ in the initial condition (70). Similar behavior was reported in the numerical examples of Refs. 9, 43-45. However, instability of the TWs is observed for large $\tau$ when hysteresis is included in the permeabilities. This requires further attention and we have excluded this possibility in our current analysis and computations.

## 5.2 | Numerical results for Scenario B

In case of Scenario B, we choose the following boundary conditions with respect to the pressure variable. As in the previous subsection, they are of Neumann type at $z = z_{in}$ and of Dirichlet type at $z = z_{out}$:

$$p'\big(z_{in}, t\big) = 0 \quad \text{and} \quad p\big(z_{out}, t\big) = p_c^{(d)}(S_B) \text{ for all } t > 0. \tag{73}$$

Moreover, the boundaries of the domain are given by: $z_{in} = -10$ and $z_{out} = 190$. To make matters interesting, contrary to the previous subsection, we do not start with an infiltration state for $S_B$, but with a drainage state. Due to the fact that we consider hysteresis both in the capillary pressure and relative permeabilities, fractional flow functions are introduced both for infiltration and for drainage. We use

$$f^{(i)}(S) = \frac{S^2}{S^2 + 3(1-S^2)}, \; f^{(d)}(S) = \frac{S^2}{S^2 + 2(1-S^2)} \text{ with } N_g = 0,$$

and define $F^{(i)}$ and $F^{(d)}$ accordingly. We verified numerically that if $S_T > S_B$ and $F^{(i)}(S_T) < F(S_B, p_B)$ then the solution is frozen in time in the sense that $S(z,t) = S(z,0)$ for all $t > 0$. This is what was discussed in Remark 8. To verify Propositions 11 and 12 and entropy solutions (66)-(69), we show two results: $S_B = S_{B,1} = 0.3$, $S_T = S_{T,1} = 0.95$, and $S_B = S_{B,2} = 0.95$, $S_T = S_{T,2} = 0.3$ both for $\tau = 0.02$. Let the corresponding solutions be $(S_{(i)}, p_{(i)})$ and $(S_{(d)}, p_{(d)})$. Since $S_{T,1} > \bar{S}_i$ for the first case (see Definition 2) and $\tau$ is small, from (67) it is expected that the entropy solution will have a shock from $S_{B,1}$ to $\bar{S}_i$, followed by a rarefaction wave from $\bar{S}_i$ to $S_{T,1}$. This is exactly what is seen from the viscous profiles obtained numerically (see Figure 23). Similarly, for the second case, since $S_{T,2} < \bar{S}_d$ and $\tau$ is small, we see from Figure 23a viscous solution resembling a drainage shock followed by a rarefaction wave, as predicted in (69). Next, we investigate whether a stable plateau is

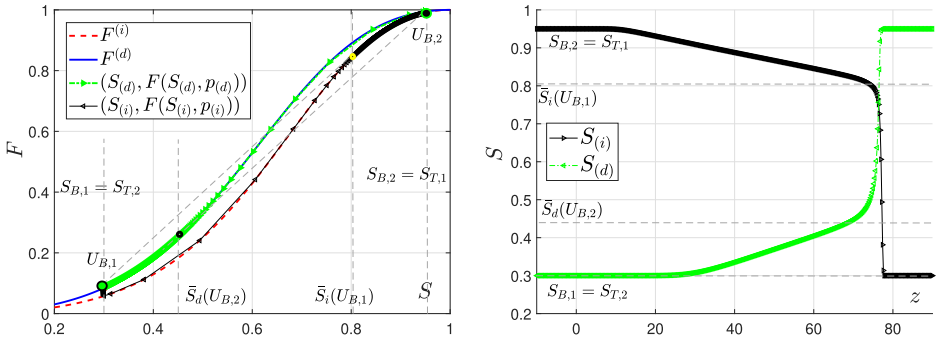


**FIGURE 23** The viscous solutions for $S_{B,1} = 0.3$, $S_{T,1} = 0.95$ denoted by $(S_{(i)}, p_{(i)})$ and $S_{B,2} = 0.95$, $S_{T,2} = 0.3$ denoted by $(S_{(d)}, p_{(d)})$ with boundary conditions (73) and $\tau = 0.02$ fixed. In the (left) plot, the solutions are shown in the $F$-$S$ plane and in the (right) plot the saturations are plotted as functions of $z$. The points $U_{B,1}$ and $U_{B,2}$ and the saturations $\bar{S}_i(U_{B,1})$ and $\bar{S}_d(U_{B,2})$, introduced in Definition 2, are marked. The results agree with the predictions of Propositions 11 and 12 and Section 4.3

formed for suitable parameter values by an infiltration wave and an ensuing drainage wave, as predicted in Proposition 13. This happens only if $\tau > \tau_i^*(S_T)$, since in this case, a monotone connection between $(S_B, p_B)$ and $(S_T, p_c^{(i)}(S_T))$ does not exist. To this end, in the numerical experiment we have used the following parameters:

$$S_B = 0.3, \quad S_T = 0.5, \quad \text{and} \quad \tau = 0.5.$$

For a stable saturation plateau, the velocities of the infiltration wave, connecting $S_B$ and $S_P$, and the drainage wave, connecting $S_P$ and $S_T$, have to be equal, that is, if $c_{(i)}^P$ and $c_{(d)}^P$ are denoting the two wave-speeds, then

$$c_{(i)}^P = \frac{F^{(i)}(S_P) - F^{(d)}(S_B)}{S_P - S_B} = \frac{F^{(i)}(S_P) - F^{(d)}(S_T)}{S_P - S_T} = c_{(d)}^P,$$

where $S_P$ stands for the saturation of the plateau. Geometrically, this equality is fulfilled, if the points

$$\big(S_B, F\big(S_B, p_B\big)\big), \big(S_T, F^{(d)}\big(S_T\big)\big) \quad \text{and} \quad \big(S_P, F^{(i)}\big(S_P\big)\big)$$

are located on the same line. This is precisely the condition that the solutions $(S_{(i)}^P, p_{(i)}^P)$ and $(S_{(d)}^P, p_{(d)}^P)$ of Proposition 13 satisfy. Drawing a line through the given points for $S_B = 0.3$ and $S_T = 0.5$ (see Figure 24), we obtain that a stable plateau should be located at $S_P \approx 0.634$. As seen from Figure 24, the orbit in the $S$-$F$ plane stabilizes exactly at $S_P \approx 0.634$ and all the three points line up. Considering Figure 25, we observe that the saturation plateau is in a transient state in the beginning, but it stabilizes at $S_P \approx 0.634$ for longer times, as the speeds of the infiltration and drainage waves match.

## 6 | FINAL REMARKS AND COMPARISON WITH EXPERIMENTS

In this work, a one-dimensional two-phase flow model has been analyzed for infiltration problems. For simplicity, we have assumed that the medium is homogeneous and a constant total velocity is prescribed at the boundary. Dynamic and hysteretic effects are included in the capillary pressure with

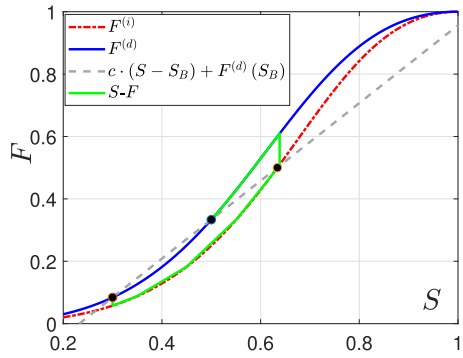


**FIGURE 24** The orbit in the $S - F$ plane representing a stable saturation plateau for Scenario B. The equilibrium points for this orbit are shown on the flux curves

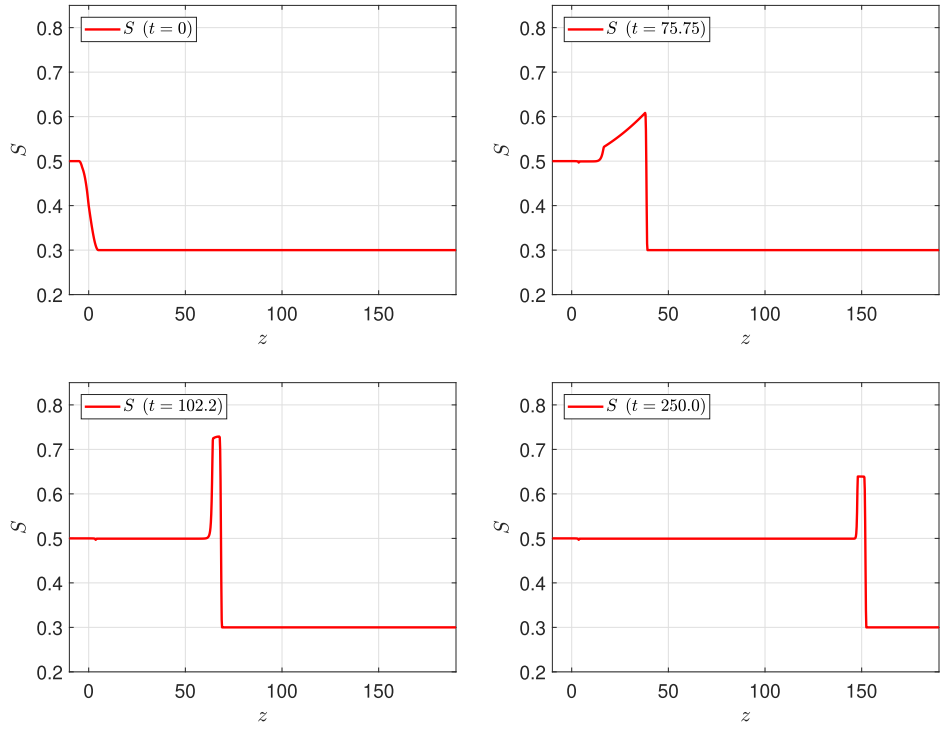


**FIGURE 25** Saturation profiles for different time points. Besides the initial condition (top left) and the final saturation profile (bottom right), two intermediate profiles are shown, which have the form of a plateau. Contrary to the final saturation profile their plateaus are not stable, since the speeds of the infiltration and the drainage fronts are equal only for $S_P = 0.634$

transitions between drainage and infiltration processes being modeled by a play-type hysteresis model having vertical scanning curves. Relative permeabilities are modeled as functions of saturation and capillary pressure to make their hysteretic nature explicit.

The focus being on TWs, the system of partial differential equations is transformed into a dynamical system. This system is analyzed for two different scenarios, A and B. In Scenario A, the hysteresis appears only in the capillary pressure, and we consider a broad range of dynamic capillarity terms,

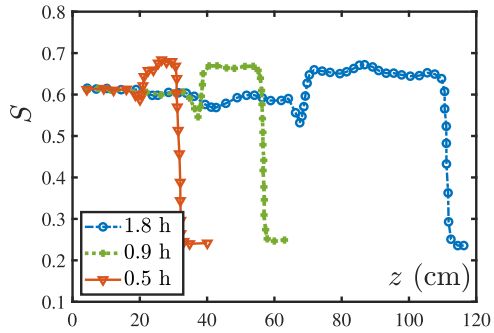


**FIGURE 26** The saturation profiles for water injection experiments taken from Ref. 29. Note the presence of growing saturation plateaus

from small to large ones. In Scenario B, hysteresis is included in both the relative permeabilities and in the capillary pressure, whereas the dynamic capillary effects are kept small. For each scenario, the existence of TW solutions is studied. In particular, we show that if the dynamic capillary effects exceed a certain threshold value, the TW profiles become nonmonotonic. Such results complement the analysis in Refs. 9, 42, 45 done for the unsaturated flow case, respectively, in Refs. 43, 44 for two-phase flow but without hysteresis. From practical point of view, the present analysis provides a criterion for the occurrence of overshoots in two-phase infiltration experiments.

Based on the TW analysis, we give admissibility conditions for shock solutions to the hyperbolic limit of the system. Motivated by the hysteretic and dynamic capillarity effects, such solutions do not satisfy the classical entropy condition. This is because the standard entropy solutions to hyperbolic two-phase flow models are obtained as limits of solutions to classical two-phase flow models, thus not including hysteresis and dynamic capillarity. In particular, for the infiltration case of Scenario A, apart from the classical solutions, there can be solutions consisting of (a) an infiltration shock followed by a rarefaction wave having nonmatching speeds, or (b) an infiltration shock followed by a drainage shock resulting in a growing saturation plateau (overshoot) in between. This is similar to the results in Refs. 43, 44. In Scenario B, the entropy solutions are shown to depend also on the initial pressure. In particular, if certain parametric conditions are met, the solutions may include ones featuring a stable saturation plateau between an infiltration front and a drainage front, both traveling with the same velocity. Such solutions are obtained, for example, in Ref. 15, but only after generating the overshoot through a change in the boundary condition. All cases mentioned above have been reproduced by numerical experiments, in which a good resemblance has been observed between the TW results and the long-time behavior of the solutions to the original system of partial differential equations.

From practical point of view, we note that the present analysis can also be used to explain experimental results reported, for example, in Refs. 33, 41, 55, 66. The occurrence of saturation overshoots is predicted theoretically for high enough dynamic capillary effects, namely, of the $\tau$ value in (24). In dimensionless setting, this can be assimilated to an injection rate that is sufficiently large. This is in line with the experimental results in Ref. 33, where the development of plateau-like profiles was observed for high enough injection rates, as shown in fig. 5 of 33 and fig. 5.3 of Ref. 66. Similarly, in the water and oil case, the plateaus are seen to develop and grow in figs. 5-6, 8-9, 18 of Ref. 29 (see Figure 26). This behavior is predicted by the analysis in Section 3. Moreover, fig. 10 of 29 might be presenting the case when the saturation has developed a plateau between two fronts traveling with the same velocity, a situation that is explained by the authors by means of hysteretic effects in the flux functions. Such solutions are investigated numerically in Refs. 15, 60, where it is shown that the plateaus can persist in

time but without explaining how they are generated. The results in Section 4 partly support the conclusions there, but also explain the mechanism behind the development of such plateaus. We mention[78] in this regard, where the authors conclude that a similar mechanism must be responsible for observed stable saturation plateaus inside viscous fingers.

## ACKNOWLEDGMENTS

K. Mitra is supported by TU Dortmund University, and was partly supported by the Netherlands Organisation for Scientific Research (NWO) through the CSER programme (project 14CSER016) and by Hasselt University, Belgium through the project BOF17BL04. I.S. Pop is supported by the Research Foundation-Flanders (FWO), Belgium through the Odysseus programme project G0G1316N and the project G051418N. The work of T. Köppl and R. Helmig is supported by the Cluster of Excellence in Simulation Technology (EXC 310/2) of Stuttgart University. Furthermore, C.J. van Duijn and R. Helmig acknowledge the support of the Darcy Center of Utrecht University and Eindhoven University of Technology and the support of the Deutsche Forschungsgemeinschaft (DFG, German Research Foundation), SFB 1313, Project Number 327154368.

## ORCID

*K. Mitra* https://orcid.org/0000-0002-8264-5982

## REFERENCES

1. Bear J. *Hydraulics of Groundwater*. New York: McGraw-Hill International Book Co.; 1979.
2. Helmig R. *Multiphase Flow and Transport Processes in the Subsurface: A Contribution to the Modeling of Hydrosystems*. Berlin: Springer-Verlag; 1997.
3. Richards LA. Capillary conduction of liquids through porous mediums. *J Appl Phys*. 1931;1(5):318-333.
4. Beliaev A, Hassanizadeh SM. A theoretical model of hysteresis and dynamic effects in the capillary relation for two-phase flow in porous media. *Transp Porous Media*. 2001;43(3):487-510.
5. Morrow N, Harris C. Capillary equilibrium in porous materials. *Soc Pet Eng J*. 1965;5(1):15-24.
6. Poulovassilis A. Hysteresis of pore water in granular porous bodies. *Soil Sci*. 1970;109(1):5-12.
7. Zhuang L, Bezerra Coelho CR, Hassanizadeh SM, van Genuchten MT. Analysis of the hysteretic hydraulic properties of unsaturated soil. *Vadose Zone J*. 2017;16(5):1-9.
8. Cao X, Pop IS. Two-phase porous media flows with dynamic capillary effects and hysteresis: uniqueness of weak solutions. *Comput Math Appl*. 2015;69(7):688-695. http://www.sciencedirect.com/science/article/pii/S0898122115000620.
9. van Duijn CJ, Mitra K, Pop IS. Travelling wave solutions for the Richards equation incorporating non-equilibrium effects in the capillarity pressure. *Nonlinear Anal Real World Appl*. 2018;41(Supplement C):232-268. http://www.sciencedirect.com/science/article/pii/S1468121817301621.
10. Behi-Gornostaeva EE, Mitra K, Schweizer B. Traveling wave solutions for the Richards equation with hysteresis. *IMA J Appl Math*. 2019;84(4):797-812. https://doi.org/10.1093/imamat/hxz015.
11. Schweizer B. The Richards equation with hysteresis and degenerate capillary pressure. *J Differ Equ*. 2012;252(10):5594-5612. http://www.sciencedirect.com/science/article/pii/S0022039612000502.
12. Rätz A, Schweizer B. Hysteresis models and gravity fingering in porous media. *Z Angew Math Mech*. 2014;94(7-8):645-654.
13. Zhang H, Zegeling PA. A numerical study of two-phase flow models with dynamic capillary pressure and hysteresis. *Transp Porous Media*. 2017 Jan;116(2):825-846. https://doi.org/10.1007/s11242-016-0802-z.
14. Papafotiou A, Sheta H, Helmig R. Numerical modeling of two-phase hysteresis combined with an interface condition for heterogeneous porous media. *Comput Geosci*. 2010;14(2):273-287.
15. Schneider M, Köppl T, Helmig R, Steinle R, Hilfer R. Stable propagation of saturation overshoots for two-phase flow in porous media. *Transp Porous Media*. 2018;121(3):621-641.

16. Brokate M, Botkin ND, Pykhteev OA. Numerical simulation for a two-phase porous medium flow problem with rate independent hysteresis. *Physica B Condense Matter*. 2012;407(9):1336-1339.
17. Philip JR. Similarity hypothesis for capillary hysteresis in porous materials. *J Geophys Res*. 1964;69(8):1553-1562.
18. Mualem Y. A conceptual model of hysteresis. *Water Resour Res*. 1974;10(3):514-520. http://doi.org/10.1029/WR010i003p00514.
19. Parker JC, Lenhard RJ, Kuppusamy T. A parametric model for constitutive properties governing multiphase flow in porous media. *Water Resour Res*. 1987;23(4):618-624.
20. Hassanizadeh SM, Gray WG. Mechanics and thermodynamics of multiphase flow in porous media including interphase boundaries. *Adv Water Resour*. 1990;13(4):169-186. http://www.sciencedirect.com/science/article/pii/030917089090040B.
21. Hassanizadeh SM, Gray WG. Toward an improved description of the physics of two-phase flow. *Adv Water Resour*. 1993;16(1):53-67.
22. Pop IS, van Duijn CJ, Niessner J, Hassanizadeh SM. Horizontal redistribution of fluids in a porous medium: the role of interfacial area in modeling hysteresis. *Adv Water Resour*. 2009;32(3):383-390.
23. Niessner J, Hassanizadeh SM. A model for two-phase flow in porous media including fluid-fluid interfacial area. *Water Resour Res*. 2008;44(8), W08439, https://doi.org/10.1029/2007WR006721.
24. Duijn CJV, Mitra K. Hysteresis and horizontal redistribution in porous media. *Transp Porous Media*. 2018;122(2):375-399. https://doi.org/10.1007/s11242-018-1009-2.
25. Gray WG, Miller CT. TCAT analysis of capillary pressure in non-equilibrium, two-fluid-phase, porous medium systems. *Adv Water Resour*. 2011;34(6):770-778.
26. Miller CT, Bruning K, Talbot CL, McClure JE, Gray WG. Nonhysteretic capillary pressure in two-fluid porous medium systems: definition, evaluation, validation, and dynamics. *Water Resour Res*. 2019;55(8):6825-6849.
27. Mitra K. *Mathematical Complexities in Porous Media Flow*. Eindhoven University of Technology & Hasselt University; 2019.
28. Schweizer B. Laws for the capillary pressure in a deterministic model for fronts in porous media. *SIAM J Math Anal*. 2005;36(5):1489-1521.
29. Gladfelter RE, Gupta SP. Effect of fractional flow hysteresis on recovery of tertiary oil. *Soc Pet Eng J*. 1980;20(6):508-520.
30. Braun EM, Holland RF. Relative permeability hysteresis: Laboratory measurements and a conceptual model. *SPE Reserv Eng*. 1995;10(03):222-228.
31. Killough JE. Reservoir simulation with history-dependent saturation functions. *Soc Pet Eng J*. 1976;16(01):37-48.
32. Topp GC, Miller EE. Hysteretic moisture characteristics and hydraulic conductivities for glass-bead media. *Soil Sci Soc Am J*. 1966;30(2):156-162.
33. DiCarlo DA. Experimental measurements of saturation overshoot on infiltration. *Water Resour Res*. 2004;40(4), W04215, https://doi.org/10.1029/2003WR002670.
34. Bottero S, Hassanizadeh SM, Kleingeld PJ, Heimovaara TJ. Nonequilibrium capillarity effects in two-phase flow through porous media at different scales. *Water Resour Res*. 2011;47(10), W10505, https://doi.org/10.1029/2011WR010887.
35. Shiozawa S, Fujimaki H. Unexpected water content profiles under flux-limited one-dimensional downward infiltration in initially dry granular media. *Water Resour Res*. 2004;40(7), W07404, https://doi.org/10.1029/2003WR002197.
36. Egorov AG, Dautov RZ, Nieber JL, Sheshukov AY. Stability analysis of gravity-driven infiltrating flow. *Water Resour Res*. 2003;39(9), 1266, https://doi.org/10.1029/2002WR001886.
37. Van Duijn CJ, Pieters GJM, Raats PAC. Steady flows in unsaturated soils are stable. *Transport Porous Media*. 2004;57(2):215-244.
38. Schweizer B. Instability of gravity wetting fronts for Richards equations with hysteresis. *Interfaces Free Bound*. 2012;14(1):37-64.
39. Hassanizadeh SM, Gray WG. Thermodynamic basis of capillary pressure in porous media. *Water Resour Res*. 1993;29(10):3389-3405.
40. Camps-Roach G, O'Carroll DM, Newson TA, Sakaki T, Illangasekare TH. Experimental investigation of dynamic effects in capillary pressure: grain size dependency and upscaling. *Water Resour Res*. 2010;46(8), W08544, https://doi.org/10.1029/2009WR008881.

41. Kalaydjian FJM. Dynamic capillary pressure curve for water/oil displacement in porous media: theory vs. experiment. In: *SPE Annual Technical Conference and Exhibition*. Society of Petroleum Engineers; 1992.
42. Cuesta C, van Duijn CJ, Hulshof J. Infiltration in porous media with dynamic capillary pressure: travelling waves. *Eur J Appl Math*. 2000;11(4):381-397.
43. van Duijn CJ, Peletier LA, Pop IS. A new class of entropy solutions of the Buckley–Leverett equation. *SIAM J Math Anal*. 2007;39(2):507-536.
44. van Duijn CJ, Fan Y, Peletier LA, Pop IS. Travelling wave solutions for degenerate pseudo-parabolic equations modelling two-phase flow in porous media. *Nonlinear Anal Real World Appl*. 2013;14(3):1361-1383.
45. Mitra K, van Duijn CJ. Wetting fronts in unsaturated porous media: the combined case of hysteresis and dynamic capillary pressure. *Nonlinear Anal Real World Appl*. 2019;50:316-341. http://www.sciencedirect.com/science/article/pii/S1468121818306254.
46. Cao X, Pop IS. Degenerate two-phase porous media flow model with dynamic capillarity. *J Differ Equ*. 2016;260(3):2418-2456.
47. Cao X, Pop IS. Uniqueness of weak solutions for a pseudo-parabolic equation modeling two phase flow in porous media. *Appl Math Lett*. 2015;46:25-30.
48. Mikelić A. A global existence result for the equations describing unsaturated flow in porous media with dynamic capillary pressure. *J Differ Equ*. 2010;248(6):1561-1577.
49. Böhm M, Showalter RE. Diffusion in fissured media. *SIAM J Math Anal*. 1985;16(3):500-509.
50. Karpinski S, Pop IS. Analysis of an interior penalty discontinuous Galerkin scheme for two phase flow in porous media with dynamic capillary effects. *Numer Math*. 2017;136(1):249-286.
51. Cao X, Nemadjieu SF, Pop IS. Convergence of an MPFA finite volume scheme for a two-phase porous media flow model with dynamic capillarity. *IMA J Numer Anal*. 2018;39(1):512-544.
52. Karpinski S, Pop IS, Radu FA. Analysis of a linearization scheme for an interior penalty discontinuous Galerkin method for two-phase flow in porous media with dynamic capillarity effects. *Int J Numer Methods Eng*. 2017;112(6):553-577.
53. Cao X, Mitra K. Error estimates for a mixed finite element discretization of a two-phase porous media flow model with dynamic capillarity. *J Comput Appl Math*. 2019;353:164-178. http://www.sciencedirect.com/science/article/pii/S0377042718307532.
54. Ewing RE. Time-stepping Galerkin methods for nonlinear Sobolev partial differential equations. *SIAM J Numer Anal*. 1978;15(6):1125-1150.
55. Glass RJ, Steenhuis TS, Parlange JY. Mechanism for finger persistence in homogeneous, unsaturated, porous media: theory and verification. *Soil Sci*. 1989;148(1):60-70.
56. Rezanezhad F, Vogel HJ, Roth K. Experimental study of fingered flow through initially dry sand. *Hydrol Earth System Sci Discuss*. 2006;3(4):2595-2620.
57. Spayd K, Shearer M. The Buckley–Leverett equation with dynamic capillary pressure. *SIAM J Appl Math*. 2011;71(4):1088-1108.
58. Bedjaoui N, LeFloch PG. Diffusive–dispersive traveling waves and kinetic relations: part I: nonconvex hyperbolic conservation laws. *J Differ Equ*. 2002;178(2):574-607.
59. El GA, Hoefer MA, Shearer M. Dispersive and diffusive-dispersive shock waves for nonconvex conservation laws. *SIAM Rev*. 2017;59(1):3-61.
60. Hilfer R, Steinle R. Saturation overshoot and hysteresis for twophase flow in porous media. *Eur Phys J Spec Top*. 2014;223(11):2323-2338.
61. Plohr B, Marchesin D, Bedrikovetsky P, Krause P. Modeling hysteresis in porous media flow via relaxation. *Comput Geosci*. 2001;5(3):225-256.
62. Schaerer CE, Marchesin D, Sarkis M, Bedrikovetsky P. Permeability hysteresis in gravity counterflow segregation. *SIAM J Appl Math*. 2006;66(5):1512-1532.
63. Bedrikovetsky P, Marchesin D, Ballin PR. Mathematical model for immiscible displacement honouring hysteresis. In: *SPE Latin America/Caribbean Petroleum Engineering Conference*. Society of Petroleum Engineers; 1996.
64. Abreu E, Bustos A, Ferraz P, Lambert W. A relaxation projection analytical-numerical approach in hysteretic two-phase flows in porous media. *J Sci Comput*. 2019;79(3):1936-1980.
65. Shearer M, Spayd KR, Swanson ER. Traveling waves for conservation laws with cubic nonlinearity and BBM type dispersion. *J Differ Equ*. 2015;259(7):3216-3232.

66. Zhuang L. *Advanced Theories of Water Redistribution and Infiltration in Porous Media: Experimental Studies and Modeling*. University of Utrecht, Dept. of Earth Sciences; 2017.
67. Leverett MC. Capillary behavior in porous solids. *Trans AIME*. 1941;142(1):152-169.
68. Graf M, Kunzinger M, Mitrovic D, Vujadinovic D. A vanishing dynamic capillarity limit equation with discontinuous flux. arXiv preprint arXiv:180502723; 2018.
69. Manthey S, Hassanizadeh SM, Helmig R, Hilfer R. Dimensional analysis of two-phase flow including a rate-dependent capillary pressure–saturation relationship. *Adv Water Resour*. 2008;31(9):1137-1150.
70. Oleinik OA. Discontinuous solutions of non-linear differential equations. *Uspekhi Mate Nauk*. 1957;12(3):3-73.
71. LeFloch PG. *Hyperbolic Systems of Conservation Laws: The Theory of Classical and Nonclassical Shock Waves*. Springer Science & Business Media; Basel 2002.
72. Brooks RH, Corey AT. Properties of porous media affecting fluid flow. *J Irrig Drain Div*. 1966;92(2):61-90.
73. Pop IS, Radu FA, Knabner P. Mixed finite elements for the Richards equation: linearization procedure. *J Comput Appl Math*. 2004;168(1):365-373.
74. List F, Radu FA. A study on iterative methods for solving Richards' equation. *Comput Geosci*. 2016;20(2):341-353.
75. Mitra K, Pop IS. A modified L-scheme to solve nonlinear diffusion problems. *Comput Math Appl*. 2019;77(6):1722-1738. http://www.sciencedirect.com/science/article/pii/S0898122118305546.
76. Cuesta C, Hulshof J. A model problem for groundwater flow with dynamic capillary pressure: stability of travelling waves. *Nonlinear Anal Theory Methods Appl*. 2003;52(4):1199-1218.
77. Nieber JL, Dautov RZ, Egorov AG, Sheshukov AY. Dynamic capillary pressure mechanism for instability in gravity-driven flows, review and extension to very dry conditions. *Transport Porous Media*. 2005; 58(1-2): 147-172.
78. Kacimov AR, Yakimov ND. Nonmonotonic moisture profile as a solution of Richards' equation for soils with conductivity hysteresis. *Adv Water Resour*. 1998;21(8):691-696.

**How to cite this article:** Mitra K, Köppl T, Pop IS, van Duijn CJ, Helmig R. Fronts in two-phase porous media flow problems: The effects of hysteresis and dynamic capillarity. *Stud Appl Math*. 2020;144:449–492. https://doi.org/10.1111/sapm.12304

## APPENDIX A: PROOFS OF SOME RESULTS GIVEN IN SECTION 3.1

*Proof of Proposition* 1. The property that $\gamma(\alpha)$ increases follows directly from (36). Moreover, $\gamma(\alpha) > \alpha$ for $\alpha > S_B$, since $\int_{S_B}^{\alpha} \mathcal{G}(S; S_B, \alpha) dS < 0$ in this case (see (37)). Observe that, if (39) is satisfied then $\gamma(\tilde{S}) < 1$. This shows the existence of $\gamma(\alpha)$ in a right neighborhood of $S = \tilde{S}$. The solution in this case exists up to $\alpha = S_* \in (\tilde{S}, \bar{S})$ where $\gamma(\alpha)$ and $\beta(\alpha)$ intersect: $\gamma(S_*) = \beta(S_*) =: S^*$.

For $S_B \in (\underline{S}, S_o)$, $\beta(\alpha)$ and $\gamma(\alpha)$ can similarly be defined, although the domain where $\beta(\alpha)$ is defined is different. In this case, the intersection of $\beta(\alpha)$ and the second solution $\gamma(\alpha)$ is guaranteed irrespective of (39) since $\int_{S_B}^{\bar{S}} \mathcal{G}(S; S_B, \bar{S}) dS < 0$ and $\int_{S_B}^{1} \mathcal{G}(S; S_B, 1) dS > 0$. This is because $\mathcal{G}(S; S_B, \bar{S}) < 0$ for $S_B < S < \bar{S}$ and $\mathcal{G}(S; S_B, 1) > 0$ for $S_B < S < 1$. ■

*Proof of Proposition* 3.

*(a)* The lower bound follows from Proposition 2. To show the upper bound, observe that if $S_m(\tau, S_T) \geq \gamma(S_T)$, then $w(\gamma(S_T)) \leq p_c^{(i)}(\gamma(S_T))$. This directly contradicts the strict inequality in (45) since $\Phi(\gamma(S_T)) = 0$.

*(b)* Since $\mathcal{G}(\cdot; S_B, S_T) < 0$ in $(\beta(S_T), 1)$, Proposition 2 and (45), (46a) imply $S_m(\tau, S_T) = 1$. Since (45) holds for all $S < 1$ and since $w' < 0$ in a left neighborhood of $S = 1$, let us suppose that $\lim_{S \nearrow 1} w(S; \tau, S_T) = -L$ $(L > 0)$. Then Equation (43) and property (39) give $w' \notin L^1$ near $S = 1$, contradicting the boundedness of $w$. ■

*Proof of Proposition* 4. We argue as in Refs. 43,44. The key idea is to introduce the function

$$u = \frac{(p_c^{(i)} - w)}{\sqrt{d}} \text{ with } d = c(S_T)\tau. \tag{A1}$$

Using (43) one obtains for $u$ the equation

$$u'(S;\tau,S_T) = \frac{1}{\sqrt{d}} p_c^{(i)\prime}(S) - \frac{\mathcal{G}(S;S_B,S_T)}{u(S;\tau,S_T)}. \tag{A2}$$

Clearly, $u|_{S_B} = 0$ and $u > 0$ in a right neighborhood of $S_B$. Since $\mathcal{G}|_{S_B} = 0$ as well, one finds from (A2) and the sign of $u$

$$u'(S_B;\tau,S_T) = \frac{p_c^{(i)\prime}(S_B)}{2}\left[\sqrt{\frac{1}{d} - 4\frac{\mathcal{G}'(S_B;S_B,S_T)}{(p_c^{(i)\prime}(S_B))^2}} - \frac{1}{\sqrt{d}}\right] > 0$$

since $\mathcal{G}'(S_B;S_B,S_T) < 0$. Using (36), Remark 3 and some elementary algebra

$$u'(S_B;\tau_1,S_T) < u'(S_B;\tau_2,S_T) \quad \text{in case } (a), \tag{A3a}$$

$$u'(S_B;\tau,S_{T,1}) < u'(S_B;\tau,S_{T,2}) \quad \text{in case } (b). \tag{A3b}$$

*(a)* From (A3a), $u_1(\cdot) := u(\cdot;\tau_1,S_T) < u(\cdot;\tau_2,S_T) =: u_2(\cdot)$ in a right neighborhood of $S_B$. We claim that $u_1$ and $u_2$ do not intersect in $\{u_1 > 0\}$. Suppose, to the contrary, there exists $S_i > S_B$ such that $u_1(S) < u_2(S)$ for $S_B < S < S_i$ and $u_1(S_i) = u_2(S_i)$. Thus ${u_1}'(S_i) \geq {u_2}'(S_i)$. Evaluating (A2) at $S_i$ gives

$${u_1}'(S_i) = \frac{p_c^{(i)\prime}(S_i)}{\sqrt{d_1}} - \frac{\mathcal{G}(S_i;S_B,S_{T,1})}{u_1(S_i)} < \frac{p_c^{(i)\prime}(S_i)}{\sqrt{d_2}} - \frac{\mathcal{G}(S_i;S_B,S_{T,2})}{u_2(S_i)} = {u_2}'(S_i),$$

a contradiction. If $S_T < S_m(\tau_2,S_T) \leq \beta(S_T)$, the $u$-monotonicity gives $S_m(\tau_1,S_T) \leq S_m(\tau_2,S_T)$. We rule out the equality by contradiction. Suppose $S_m(\tau_1,S_T) = S_m(\tau_2,S_T) =: S_m$. Then

$$u_1 < u_2 \text{ in } (S_B,S_m).$$

Integrating Equation (A2) from $S_T$ to $S_m$ gives

$$u_2(S_T) - u_1(S_T) = (p_c^{(i)}(S_T) - p_c^{(i)}(S_m))\left(\frac{1}{\sqrt{d_2}} - \frac{1}{\sqrt{d_1}}\right) + \int_{S_T}^{S_m} \mathcal{G}\left(\frac{1}{u_2} - \frac{1}{u_1}\right). \tag{A4}$$

Since $\mathcal{G} > 0$ in $(S_T,S_m)$ for $S_T < S_m \leq \beta(S_T)$, the term in the right of (A4) is negative, yielding a contradiction.

*(b)* Using (36), this part is demonstrated along the same lines. Details are omitted. ■

*Proof of Proposition* 5. As seen from (A2), $v$ satisfies the equation

$$(v^2)' = 2vp_c^{(i)\prime} - 2c\tau\mathcal{G} \text{ in } \{v > 0\}.$$

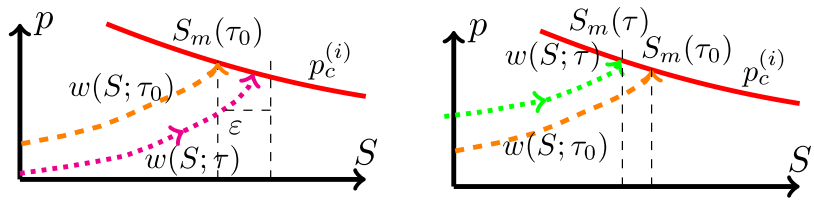


**FIGURE A1** Behavior of $w$ close to $S_m$: (left) $\tau > \tau_0$ and (right) $\tau < \tau_0$

Integrating this equation and using Proposition 4 and $\Phi$ from (45) gives the desired inequalities. ■

*Proof of Corollary* 1. We only demonstrate continuity with respect to $\tau$. The proof of continuity with respect to $S_T$ follows the same arguments. We therefore take $S_T = S_{T_0}$ and drop its dependence from the notation for simplicity. Consider first $\tau > \tau_0$ and $S_{T_0} < \beta(S_{T_0})$. Recalling $v(S_m(\tau_0);\tau_0) = 0$, Proposition 5 gives

$$0 < v(S_m(\tau_0);\tau) < \sqrt{2c(\tau-\tau_0)\Phi(S_m(\tau_0))},$$

where $\Phi(S_m(\tau_0)) > 0$ by (46) and Proposition 3. For any given (small) $\varepsilon > 0$ and with reference to Figure A1 choosing $\delta < \frac{p_c^{(i)}(S_m(\tau_0)) - p_c^{(i)}(S_m(\tau_0)+\varepsilon)}{2c\Phi(S_m(\tau_0))}$ we have

$$w(S_m(\tau_0),\tau) > p_c^{(i)}(S_m(\tau)+\varepsilon) \text{ for all } \tau - \tau_0 < \delta.$$

Since $w' > 0$, this implies the continuity of $\tau > \tau_0$.

Next let $\tau < \tau_0$ and $S_{T_0} \le \beta(S_{T_0})$. Now we have from Proposition 5

$$0 < v(S_m(\tau);\tau_0) < \sqrt{2c(\tau_0-\tau)\Phi(S_m(\tau))}. \tag{A5}$$

Since $v(\cdot,\tau_0) \in C([S_B, S_m(\tau_0)])$, $v(S_m(\tau_0),\tau_0) = 0$ and $v(\cdot,\tau_0) > 0$ in $(S_B, S_m(\tau_0))$, the continuity of $S_m$ follows directly from (A5). ■

*Proof of Proposition* 7.

*(a)* Suppose no $\tau_c(S_T)$ exists such that $S_m(\tau_c, S_T) = \beta(S_T)$, meaning $S_m(\tau, S_T) < \beta(S_T)$ for all $\tau > 0$. From [Ref. 9, proposition 4.2(b)] we have that

$$w(S;\tau,S_T) \to -\infty \text{ as } \tau \to \infty \text{ for all } S \in (S_B, S_T].$$

This implies that for large enough $\tau$, a $S_1 \in [S_T, \beta(S_T)]$ exists for which $w(S_1) = 0$. From (43), it is evident that $w(S_T) \le w(S)$, in particular $w(S_T) < w(S_1) = 0$. Moreover, (45) gives the lower bound $w(S) \ge w(S_T) \ge p_c^{(i)}(S_T) - \sqrt{2c\tau\Phi(S_T)} \ge -\sqrt{2c\tau\Phi(S_T)}$ for all $S \in [S_B, S_m(\tau, S_T)]$. Multiplying both sides of (A2) by $u$, integrating from $S_B$ to $S_1$ and using the above inequality we get

$$\begin{aligned} -\frac{1}{2}p_c^{(i)2}(S_B) &= \int_{S_B}^{S_1} (c\tau\mathcal{G}(S;S_B,S_T) + p_c^{(i)\prime}(S)w(S;c,\tau))dS \\ &\le -c\tau\Phi(S_1) + (p_c^{(i)}(S_B) - p_c^{(i)}(S_1))\sqrt{2c\tau\Phi(S_T)}. \end{aligned}$$

Since $\Phi(S_1) > 0$ (as stated in (46b)), this leads to a contradiction for $\tau \to \infty$. Hence, $S_m(\tau, S_T) = \beta(S_T)$ for some $\tau > 0$. The uniqueness follows from Proposition 4.

*(b)* The monotonicity and continuity follows from Propositions 4 and 5 and Corollary 1. To show the limit for $S_T \searrow S_*$, assume that $\lim_{S_T \searrow S_*} \tau_c(S_T) = \tau_\infty < \infty$. Let then $\tau > \tau_\infty$. Proposition 3 implies that $S_m(\tau, S_*) < \beta(S_*)$. Choose an $S_T > S_*$ such that $\beta(S_T) \geq S_m(\tau, S_*)$. Since $\tau > \tau_c(S_T)$, we get that $w(S_m(\tau, S_*); \tau, S_T) \leq w(\beta(S_T); \tau, S_T) \leq p_c^{(i)}(\beta(S_T))$, implying $w(S_m(\tau, S_*); \tau, S_*) - w(S_m(\tau, S_*); \tau, S_T) \geq p_c^{(i)}(S_m(\tau, S_*)) - p_c^{(i)}(\beta(S_T))$. This gives a contradiction when $S_T \searrow S_*$ since the right-hand side goes to $p_c^{(i)}(S_m(\tau, S_*)) - p_c^{(i)}(\beta(S_*)) > 0$, whereas the left-hand side converges to 0 from Corollary 1.

The existence of a $\bar{\tau} > 0$ is a consequence of the continuity of $\tau_c$ with $\bar{\tau} = \tau_m(\bar{S}) \geq \bar{\tau}_m(\bar{S})$ following from Proposition 6.

■